Journal of Geophysical Research: Solid Earth

RESEARCH ARTICLE
10.1002/2017JB014970

Special Section:
Slow Slip Phenomena and Plate Boundary Processes

Characterizing Afterslip and Ground Displacement Rate Increase Following the 2014 Iquique-Pisagua M_w 8.1 Earthquake, Northern Chile

Felix Hoffmann[1], Sabrina Metzger[1], Marcos Moreno[1,2], Zhiguo Deng[1], Christian Sippl[1], Francisco Ortega-Culaciati[3], and Onno Oncken[1,4]

[1]German Research Centre for Geosciences (GFZ), Potsdam, Germany, [2]Departamento de Geofísica, Facultad de Ciencias Físicas y Matemáticas, Universidad de Concepción, Concepción, Chile, [3]Departamento de Geofísica, Universidad de Chile, Santiago, Chile, [4]Institut für Geologische Wissenschaften, Freie Universität Berlin, Berlin, Germany

Key Points:
- GPS rates south of 21°S accelerate in the second year following the Iquique-Pisagua event potentially reflecting coupling increase
- Afterslip lasts about 2 years before the interface relocks again almost entirely
- GPS velocity patterns and modeled interface afterslip rates suggest a seismotectonic barrier at 21°S

Supporting Information:
- Supporting information S1

Correspondence to:
S. Metzger,
metzger@gfz-potsdam.de

Citation:
Hoffmann, F., Metzger, S., Moreno, M., Deng, Z., Sippl, C., Ortega-Culaciati, F., & Oncken, O. (2018). Characterizing afterslip and ground displacement rate increase following the 2014 Iquique-Pisagua M_w 8.1 earthquake, Northern Chile. *Journal of Geophysical Research: Solid Earth*, *123*, 4171–4192. https://doi.org/10.1002/2017JB014970

Received 11 SEP 2017
Accepted 23 MAR 2018
Accepted article online 25 MAR 2018
Published online 7 MAY 2018

Abstract The 2014 Iquique-Pisagua M_w 8.1 earthquake ruptured only parts of the 1877 Northern Chile-Southern Peru seismic gap. Here we present a comprehensive analysis of 152 continuous and campaign Global Positioning System time series that captured more than a decade of interseismic loading prior to the event and 2 years of afterslip. In high spatiotemporal resolution, our data document upper plate response not only at the coseismically affected latitudes but also at the adjacent Loa plate segment to the south. Using a combination of elastic and viscoelastic half-space models of different stages of the seismic cycle, we found that the highly coupled, former seismic gap contains a narrow low coupling zone at 21°S latitude. Just after the 2014 earthquake, this zone acts as a barrier impeding afterslip to continue southward. Possible reasons for this impediment could involve crustal heterogeneities or coupling discontinuities at the plate interface. After 2 years, afterslip cumulates to a maximum of ~89 cm and becomes negligible. Global Positioning System observations south of the inferred seismotectonic barrier reveal a deformation rate increase in the second year after the event. Our slip models suggest that this could be caused by a downdip coupling increase, perhaps bringing the highly coupled southern Loa segment closer to failure. Taken together, our results reveal (1) the interaction between different areas undergoing stress release and stress buildup in a major seismic gap, (2) constraints for the temporal variation of coupling degree in different stages of the seismic cycle, and (3) the influence of large earthquakes at adjacent segments.

1. Impact of the 2014 Earthquake on the 1877 Seismic Gap

The convergent plate boundary of western South America is characterized by megathrust events with short recurrence intervals. Almost all segments south of Peru broke within the last century and generated large subduction earthquakes such as the 1960 Valdivia M_w 9.5 earthquake (Kanamori, 1977) or the 2010 Maule M_w 8.8 earthquake (e.g., Moreno et al., 2010). The segment between 18 and 23°S latitude, known as Northern Chile-Southern Peru seismic gap, has not ruptured since 1877 (M_w 8.6 Iquique earthquake) but is capable of generating a M_w ~9 earthquake (e.g., Kelleher, 1972; Figure 1). With an estimated recurrence interval of ~100 years (Comte & Pardo, 1991) and two recent earthquakes in the adjoining segments, namely, the 1995 Antofagasta M_w 8.1 event in the south (Ruegg et al., 1996) and the 2001 Arequipa M_w 8.3 event in the north (Ruegg et al., 2001), this gap was considered to be the most mature seismic gap along the South American plate boundary south of Peru. Despite the occurrence of several smaller earthquakes in the area during the last century (Comte & Pardo, 1991; Engdahl & Villasenor, 2002) and the 2007 Tocopilla M_w 7.8 event (e.g., Motagh et al., 2010), the slip deficit remained nearly unchanged and recent geodetic studies report high plate coupling rates (e.g., Li et al., 2015; Métois et al., 2013). A megathrust event leading to a closure of the seismic gap has been expected for more than 30 years (e.g., Kelleher, 1972; Nishenko, 1985). For this reason, the region has been particularly well monitored for more than two decades already: first by the South American Geodynamic Activities project that started in 1993 (e.g., Klotz et al., 1999, 2001) and the International Associated Laboratories "Montessus de Ballore" project in the 1990's (Chlieh et al., 2004; Métois et al., 2013). Since 2007 the area has constantly been monitored by the Integrated Plate Boundary Observatory Chile (IPOC), an international effort to measure ground deformation with multipurpose instrumentation (Moreno et al., 2017) extended with University NAVSTAR Consortium data (Simons et al., 2010).

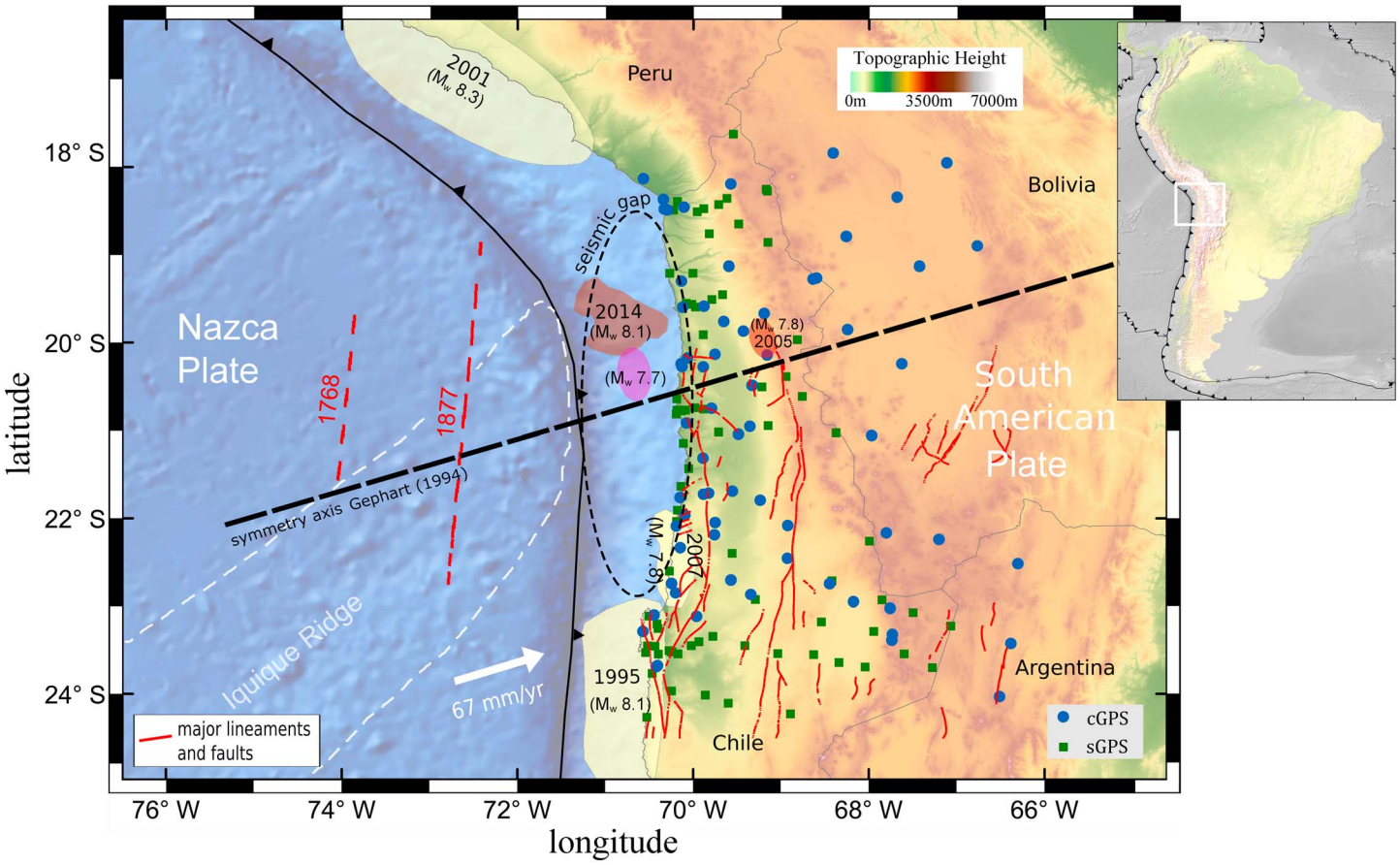

Figure 1. Topographic and geographic map of the Northern Chile-Southern Peru seismic gap region. Its relative location on the South American continent is shown in the inset. Rupture zones of past relevant earthquakes are indicated as shaded areas (source: U.S. Geological Survey): the 1995 Antofagasta, the 2001 Arequipa, the 2007 Tocopilla event (yellow), the 2005 Tarapacá event (orange), and the 2014 Iquique-Pisagua event (red) including its largest aftershock (magenta). The Northern Chile-Southern Peru Seismic gap is highlighted with a dashed ellipse. Inferred along-strike extents of the two last megathrust events in the gap area are indicated with dashed red lines (Comte & Pardo, 1991). The blue circles (continuous Global Positioning System (GPS) stations, cGPS) and green squares (survey-mode GPS stations, sGPS) mark the location of GPS stations used in this study. The Iquique Ridge is marked as dashed white line (Geersen et al., 2015). Major geologic faults and lineaments are highlighted in red (Reutter et al., 1994). The topographic symmetry axis of the Andes is indicated as black dashed line (Gephart, 1994).

On 1 April 2014, the Iquique-Pisagua M_w 8.1 megathrust event with a rupture length of about 100 km broke the plate interface in the central northern part of the gap close to the town of Pisagua (e.g., Ruiz et al., 2014; Schurr et al., 2014; see Figure 1). The mainshock nucleated in a zone of intermediate interseismic coupling and initially ruptured downdip toward a patch of higher coupling (Hayes et al., 2014; Schurr et al., 2014). Aftershocks are concentrated at the southern edge of the rupture zone (Meng et al., 2015) with the largest one being a M_w 7.7 event that occurred 2 days after and 100 km SSE of the main event (Duputel et al., 2015). Both events led to a cumulative failure of the plate interface of about 200 km length, which reflects only a partial release of the slip deficit accumulated since 1877 (Schurr et al., 2014).

In this study, we present new Global Positioning System (GPS) data acquired before and after the Iquique-Pisagua earthquake. From the acquired time series, we extract interseismic and postseismic deformation rates to analyze the temporal and spatial evolution of deformation following the earthquake. We further investigate deformation rate changes on the unbroken southern segment of the seismic gap. Interpreting surface displacements is one of the key elements in understanding the behavior of subduction zones. After a large earthquake, lithospheric stress is released in three principal processes: (1) continued slip of the fault referred to as afterslip (e.g., Marone et al., 1991; Perfettini et al., 2010), (2) poroelastic rebound due to pore fluid pressure changes (e.g., Jónsson et al., 2003; Peltzer et al., 1998), and (3) viscoelastic relaxation of the mantle (e.g., Nur & Mavko, 1974; Wang et al., 2012), while the fault simultaneously relocks during the postseismic stage. These postseismic processes may take place simultaneously and vary in duration between months to decades depending on the magnitude of the event as well as on the rheology of the

deformed material and/or the frictional properties of the slipping interface. In our analysis, we assume afterslip to be the driving mechanism controlling early postseismic deformation, although we recognize that other processes may contribute to the GPS-derived surface displacements. Of particular interest to us is the assessment of slip behavior in the postseismic stage across different tectonic segments, especially toward the southern edge of the pre-2014 seismic gap. The rupture zone of the Iquique-Pisagua event only covers less than one third of the 1877 rupture as inferred by Comte and Pardo (1991). This means that the southern segment of the Northern Chile-Southern Peru seismic gap now has accumulated a slip deficit for more than 140 years (Figure 1). For the regional earthquake hazard assessment, it is important to understand how the 2014 earthquake affects this segment of the gap. Thanks to the dense spatial coverage of GPS observations in Northern Chile (Figure 1), we can characterize regional crustal deformation in great detail. In order to evaluate spatial and temporal changes in plate coupling, we compare GPS rates before and after the Iquique-Pisagua event on the northern and southern part of the 1877 seismic gap. We first isolate tectonic GPS rates from nontectonic contributions (section 2) then use a combination of elastic and viscoelastic slip models to analyze the interseismic and postseismic stage of the Iquique-Pisagua earthquake (sections 3 and 4), discuss the interpretation of the model results (section 5), and finally draw conclusions (section 6).

2. GPS Observations and Model Approach

2.1. GPS Data Processing

The geodetic instrumentation of the IPOC (Moreno et al., 2017) and International Associated Laboratories network (Chlieh et al., 2004; Métois et al., 2013) includes GPS sites that are operated continuously (cGPS) and in survey mode (sGPS), the latter of which are also referred to as campaign GPS sites. We include data from 75 cGPS stations and 77 sGPS sites covering a latitudinal range of 17–24°S from the coast to 450 km inland (Figure 1). The sGPS sites are not strictly measured periodically but at least once every 3 years for at least 48 consecutive hours, thus delivering less accurate positioning than the cGPS stations. But since the sGPS time series extend further back in time compared to the cGPS time series, they are most helpful to estimate interseismic rates prior to the 2014 Iquique-Pisagua earthquake (Figure S1 in the supporting information).

All GPS data are organized in units of 24-h periods and were processed using the Earth Parameter and Orbit System software (Deng et al., 2016). We calibrated the positions using absolute antenna phase centers provided by the International Global Navigation Satellite System Service (Schmid et al., 2007) and compensated tidal effects using the Finite Element Solution tide model 2004 (Lyard et al., 2006). We estimated station coordinates and tropospheric wet zenith delays using random-walk parameters for every hour (Gendt et al., 2013). Finally, we estimated coordinates in network mode and aligned them to the International Global Navigation Satellite System Service combined coordinate product reducing the impact of the Earth rotation parameter (Rebischung et al., 2015). The GPS processing results are compatible with the International Terrestrial Reference Frame 2014 (Altamimi et al., 2016), which is based on a kinematic model without taking into account the nondeformational rotation of South America. We compute our final horizontal velocity field relative to the stable South American Plate by applying an Euler pole rotation (21.44°S, 125.18°W, 0.12°/Myr^{-1}, Moreno et al., 2011) comparable to the NNR-Nuvel-1A model (DeMets et al., 1994). Examples of cGPS (Figure S2) and sGPS (Figure S3) time series and more details of GPS data processing (Text S1 and Figure S4) and reference frame realization (Figure S5) are provided in the supporting information.

2.2. Extracting the Tectonic GPS Signal

Our GPS time series cover a time interval of more than a decade (1999–2016 for sGPS and 2003–2016 for cGPS; Figure S1) and include a variety of tectonic and other signals occurring at the convergent plate boundary. We excluded 3 months of data preceding the Iquique-Pisagua event 2014 from our time series as they were affected by preseismic transients (Bedford et al., 2015; see also section 3.1). The recorded ground displacements are the sum of tectonic, atmospheric, instrumental, and other signal contributions, like interseismic shortening, coseismic displacements, instrumental failure (e.g., antenna replacements), postseismic transients, and seasonal oscillations:

$$\delta_{\mathrm{GPS}}(t) = \delta_{\mathrm{interseismic}}(t) + \delta_{\mathrm{coseismic}}(t) + \delta_{\mathrm{AntennaOffset}}(t) + \delta_{\mathrm{postseismic}}(t) + \delta_{\mathrm{seasonal}}(t) \quad (1)$$

Following the approach of Metzger et al. (2013) and Bevis and Brown (2014), we simulate these signal types in our GPS displacement time series with (Figure 2)

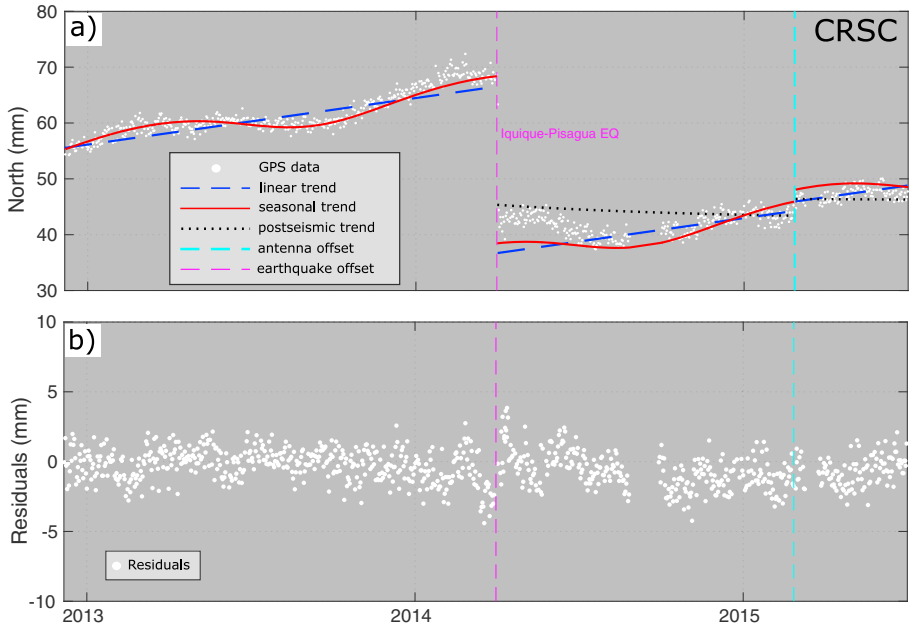

Figure 2. (a) Time series of station CRSC (see Figure 6 for location) and its decomposition into various model trajectories highlighted in different colors. (b) The model residuals of (a) (based on equation (2)). GPS = Global Positioning System.

$$\delta_{\mathrm{GPS}}(t) = [\mathrm{A} + \mathrm{B}\cdot(t - t_r)] + \left[\sum_{\mathrm{eq}=1}^{n_{\mathrm{eq}}} C_{\mathrm{eq}}\cdot H(t - t_{\mathrm{eq}})\right] + \left[\sum_{\mathrm{ao}=1}^{n_{\mathrm{ao}}} D_{\mathrm{ao}}\cdot H(t - t_{\mathrm{ao}})\right] + \left[\sum_{\mathrm{p}=1}^{n_p} E_p\cdot \log\left(1 + \frac{t - t_{\mathrm{eq}}}{T}\right)\right] + [F_1\cdot \sin(2\pi\cdot t) + F_2\cdot \cos(2\pi\cdot t) + F_3\cdot \sin(4\pi\cdot t) + F_4\cdot \cos(4\pi\cdot t)] \quad (2)$$

The constant A corrects the time series for any initial offset, and the linear term B represents a constant plate velocity in each stage of the seismic cycle (Wang et al., 2012) with respect to a predefined reference time t_r. Discontinuities can arise either from coseismic displacements (*eq*) or antenna offsets (*ao*). The mathematical approach to model such data offsets is a Heaviside function $H(t)$, where n_{eq} earthquakes (or n_{ao} antenna offsets, respectively) induce a step with amplitude C_{eq} (D_{ao}) at times t_{eq} (t_{ao}). The challenge is to distinguish artificial steps in the displacement function from earthquake-induced ground motion. Postseismic relaxation observed after n_p large earthquakes is represented by a logarithmic transient E_p with a nonlinear parameter T. Bevis and Brown (2014) showed that the logarithm is nearly insensitive to T; hence, this component can be linearized by setting T equal to 1 year. The most rapid deformation within the first weeks after the earthquake might not be perfectly represented by this simplification (Figure 2b). However, we demonstrate in section 3.1 that the linear term is most important for our velocity analysis. The last term in equation (2) represents an elastic loading response of the crust to seasonal changes in the water cycle (e.g., Heki, 2001; Van Dam et al., 2001). We apply a Fourier second-order series for terms F_1 to F_4 that represent two annual and two semiannual intervals (Dong et al., 2002).

To estimate all parameters mentioned above and to exclude irrelevant signal contributions (instrumental offsets and seasonal loading) from further analysis, we modeled the cGPS time series component wise using a least squares inversion (Figure 2). To exclude coseismic and postseismic signals related to other events than the 2014 Iquique-Pisagua earthquake, we developed a semiautomated earthquake selection procedure that extracts relevant earthquakes from the U.S. National Earthquake Information Center catalog. We used a distance-magnitude filter to identify all events that could potentially have affected our GPS time series, that is, that occurred within a radius of 20 to 2,500 km and with an incremental magnitude of 5 to 8.

All remaining offsets in the time series were then visually checked and manually classified as antenna offsets. The average rms (root-mean-square) error of all stations is 1.2 mm for the east, 1.0 mm for the north and 2.0 for the vertical component; stationwise, it ranges from 0.9 mm (LVRA) to 1.9 mm (PCAL) in the east component, 0.8 mm (ANT2) to 2.4 mm (PICN) in the north component and 1.5 mm (MCLA) to 2.7 mm (UTAR) in the

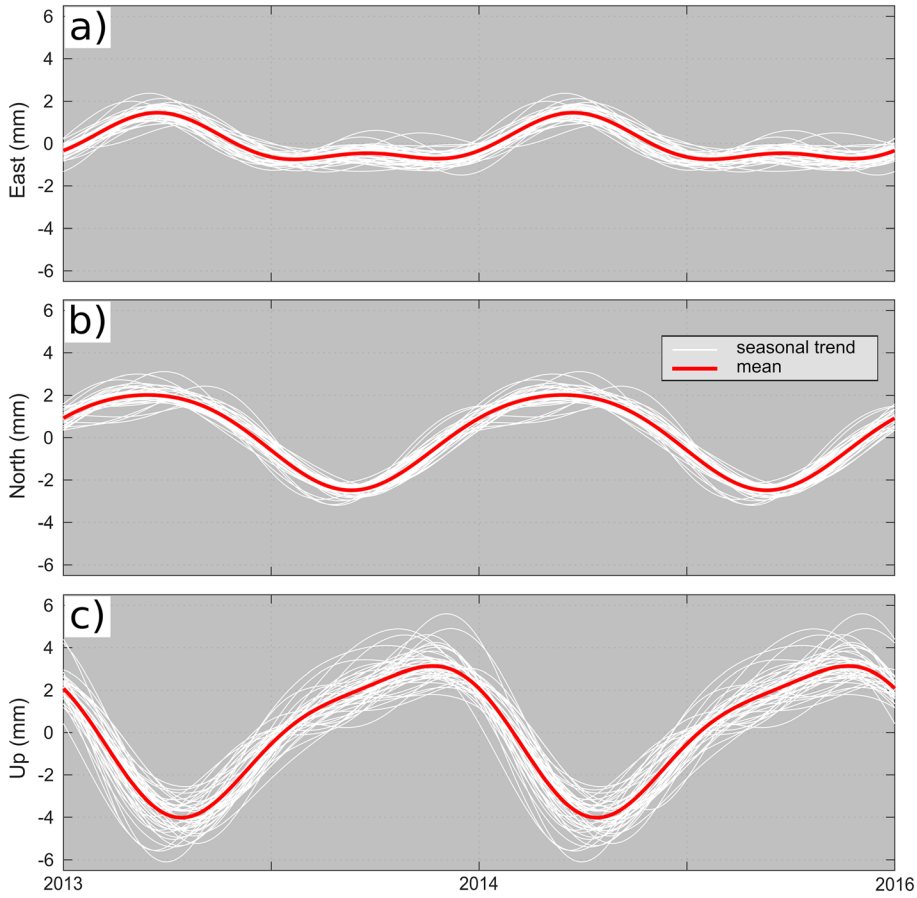

Figure 3. Modeled seasonal signal on the (a) east, (b) north, and (c) up components of 50 continuous Global Positioning System stations. Stations with significant data gaps (Figure S1b) were excluded from the analysis.

vertical component (Table S1). The residuals of the time series inversion are close to 0, thus indicating that our approach in equation (2) seems reasonable for approximating the observed GPS ground motion signal (Figure S2). We then subtracted the nontectonic signal contributions, the seasonal trend, and the antenna offsets, from the time series for each station individually (Figure S2). We further find that the seasonal changes are surprisingly consistent over the whole cGPS network (Figure 3). The east component contains a clear biannual signal with one peak in February/March and a second lower peak in September, whereas the north component exhibits a clear annual signal with a peak in February/March and a low in September. The vertical component also exhibits a one-peak annual trend, in which the highs and lows are shifted in respect to horizontal components to October/November (peak) and May/June (low).

The campaign GPS data have a much lower temporal resolution and have been collected irregularly and in different seasons (Figure S3). Thus, the extraction of the tectonic signal is more challenging here. We used the seasonal parameters estimated from the cGPS data to correct the campaign data and applied a seasonal model derived from the mean of each parameter F_1 to F_4 in equation (2) (Tables S2 and S3 and Figure S6).

2.3. Data Time Windows and Model Strategy

In order to better understand the different stages of the Northern Chile seismic cycle, we split the GPS data into an interseismic part prior to and a postseismic part after the 2014 Iquique-Pisagua earthquake. The interseismic interval is covered by three to eight GPS campaigns between 1999 and end of 2013 and by cGPS observations spanning a time interval from 2003 to end of 2013 (data from 2014 were cut due to observed GPS transients, see also section 3.1 and Figure S1). The postseismic interval contains another two to three campaign GPS surveys, covering a time period of 3 weeks after the mainshock until April 2016 and daily solutions from 3 April 2014 to April 2016. To not contaminate the afterslip analysis with the largest aftershock

occurring on 3 April, we excluded the cGPS solutions of the first 2 days after the mainshock. To analyze the temporal evolution of the postseismic response to the earthquake, we further subdivided the postseismic part into three periods that best match the timing of the campaign GPS surveys (Figure S1a). The intervals comprise days 2–16, days 17–334, and days 335–717 after the mainshock and are henceforth called Periods 1, 2, and 3, respectively.

We invert the observed GPS surface displacements for estimating slip (respectively backslip) on the subduction interface using elastic and viscoelastic half-space models (Okada, 1992). For the interseismic model, we assume elastic deformation (Okada, 1992) to be the dominant driver (e.g., Chlieh et al., 2011; Métois et al., 2016). For the postseismic models of Periods 1–3, we combine the elastic afterslip model with viscoelastic mantle relaxation using the PyLith software (Aagaard et al., 2013). In the viscoelastic finite element modeling approach, we use four different material blocks to discriminate between an elastic crust and lithospheric mantle and a viscoelastic asthenospheric mantle (Text S2 and Figure S7). The model geometry of the subducting slab is based on the SLAB 1.0 model (Hayes, Wald, & Johnson, 2012) and the elastic-visco-elastic boundary is based on the continental Moho of Tassara and Echaurren (2012). We fixed the Young's modulus to 100, 120, and 160 GPa for the continental, oceanic, and mantle layers, respectively (Li et al., 2015), and use the linear Maxwell rheology in the viscoelastic body. The Poisson's ratio is set to 0.265 and 0.30 for the continental and oceanic crust (Christensen, 1996).

In general, Maxwell viscosity is preferably applied for long-term viscosity estimates, whereas Burgers viscosity resolves short-term rheologic transients typical for the early postseismic stage (e.g., Li et al., 2015; Trubienko et al., 2013). We decided to use Maxwell rheology to reduce complexity and computational cost. When using predetermined time windows like here, the effective viscosity is defined as the best fitting Maxwell viscosity (Li et al., 2017). This approach has been successfully applied for GPS data in Chile before (Bedford et al., 2016; Li et al., 2017), but we cannot exclude the possibility that this simplification creates artifacts in our slip models as discussed in section 5. To simulate the viscous response to coseismic stress perturbation, we used the slip model of Schurr et al. (2014) and estimated the viscoelastic deformation in the respective model Periods 1–3 (Tables S7, S9, and S11). We tested different values of the Maxwell viscosity of the continental mantle and kept all other parameters constant, including the oceanic mantle viscosity, which we fixed to 10^{20} Pa s (Hu et al., 2014; Li et al., 2015). Continental viscosity was varied between 10^{18} Pa s (highly viscous) and 10^{20} Pa s (nearly elastic) in our tests and was finally constrained to 2×10^{19} Pa s, based on the best data fit (rms, see examples for Period 2 in Figures S8 and S9). Using these fixed viscosities, we removed the predicted viscoelastic signal component from our GPS observations in advance and thus account for the viscous mantle relaxation. In a second step, we subtracted the interseismic loading component from each postseismic period to finally invert for the afterslip signal only (more details can be found in section 4.1).

The elastic model geometry of the plate interface slip is also based on the SLAB1.0 subduction zone model (Hayes et al., 2012), from which we utilized the region from 17.5 to 26°S latitude. Slip is modeled as along strike and updip dislocations on 1,016 triangular fault patches with an average area of 170 km^2 and constrained to a maximum depth of 65 km, assumed to represent the Moho depth (Chlieh et al., 2011; Husen et al., 2000). We invert Green's functions describing slip at depth on the interface geometry to best fit the observed GPS displacements in a least squares approach (Okada, 1992). We do not constrain the rake, thus allowing backslip to occur. For regularization of the inversion, we applied a Laplacian smoothing, making the solution more stable while minimizing slip variations of neighboring patches based on an input smoothing weight. The strength of the regularization is determined by considering the trade-off between misfit and slip roughness (Figure S10). In the interseismic backslip model, three additional model parameters describe an Euler pole that accounts for the motion of the Central Andean sliver (Bevis et al., 2001). The sliver motion is collinear to the plate convergence and causes back-arc shortening in the Subandeans (Chlieh et al., 2011). This model modification allows to better describe the abnormally high interseismic GPS rates (with respect to the overall convergence rate in Northern Chile) that cannot be explained by an elastic response of the plate interface alone (e.g., Métois et al., 2013, 2014). The Green's functions are inverted with the MATLAB routine "lsqlin," a subspace trust-region-reflective algorithm based on the interior-reflective Newton method (Coleman & Li, 1996). To avoid physically unreasonable slip rates and additionally improve model resolution, we apply constraints for minimum slip (Du et al., 1992) based on the constant plate velocity of 67 mm/year (Angermann et al., 1999). The respective minimum slip for interseismic and postseismic models corresponds

to the "negative" backslip rates of −61 mm/year that would equal a locked (fully coupled) interface dipping 25–30° (e.g., Husen et al., 2000).

3. Interseismic Period

3.1. Constraining GPS Rates

The interseismic ground displacements in our GPS network were affected by two major earthquakes in Northern Chile (Figure S11): the 2005 Tarapacá M_w 7.8 earthquake (Delouis & Legrand, 2007; Ruiz et al., 2014) and the 2007 Tocopilla M_w 7.8 earthquake (Motagh et al., 2010; Weiss et al., 2016). We therefore excluded all data between November 2007 and January 2008, when GPS rates were dominated by afterslip from the Tocopilla event (e.g., Delouis et al., 2009) and data in May and June 2005 due to the Tarapacá event. We further excluded all GPS data in the 3 months before the Iquique-Pisagua main rupture on 1 April, 2014, where clear transient signals appear in the time series (Figure S12). These distinct features reflect either a slow slip event preceding the mainshock (e.g., Ruiz et al., 2014; Yagi et al., 2014) or represent a surface expression of precursors of seismic slip (e.g., Bedford et al., 2015; Schurr et al., 2014). We split the interseismic GPS data into three parts to investigate on rate differences in the interseismic stage: (A) a pre-Tarapacá interval with data before June 2005, (B) a time interval between the Tarapacá and the Tocopilla event from July 2005 to October 2007, and (C) a post-Tocopilla interval with all data from February 2008 to end of December 2013.

In all three parts of the time series, we removed data points with a position error above the 99.5th percentile and/or each point whose position differs from its neighbor by more than 3 times the standard deviation of the first derivative of the time series. For each of the three interseismic subsets of continuous time series longer than 1 year, we estimate the interseismic rate by extracting the linear trend from the signal as explained in section 2.2. From the sGPS data, we derived the interseismic rates using linear regression. The rate differences of the 1d-horizontal velocities between the pre-Tarapacá (A), the inter-earthquake (B), and post-Tocopilla (C) periods do not exceed 5 mm/year (Table S4). We use the mean of all three periods, equally weighted as interseismic velocity for further analysis. The resulting velocity may not fully account for interseismic transients observed in the epicenter regions of the Tarapacá and Tocopilla events (e.g., Weiss et al., 2016). Uncertainties of the resulting cGPS rate model parameters are calculated from the mean instrumental error in each model interval. Given the low number of observations, calculating campaign GPS errors is more challenging. Following Geirsson et al. (2006), we correct the rms fit by the number of model parameters (two in the linear case) and normalize it by the full length of the time series.

The resulting interseismic rates (Tables S5 and S6) were corrected for the Andean sliver motion (see sections 2.2 and 3.2 and Figure 4a). They exhibit a consistent ENE motion that is collinear to the plate convergence over the entire area of interest in Northern Chile, even in the far field of the network. The interseismic observations are characterized by a gradual rate decrease of about 7 mm per 100 km from coastal stations to stations on the Andean Plateau. Maximum horizontal GPS velocities of up to 35.3 ± 3.1 mm/year (station MEJS) occur at coastal stations at the southern edge of our GPS network at a minimum distance of ~80 km to the trench, whereas minimal horizontal GPS velocities of 14.1 ± 5.2 mm/year (PAJA) occur on the Andean Plateau at a longitude of about 67°W and ~490 km distance to the trench (Figure 4a). The rates also exhibit a north-south gradient from coastal stations close to the border to Peru that show significantly slower GPS rates of 20.3 ± 1.2 mm/year (LYAR) to coastal stations in the south like the afore mentioned station MEJS. The vertical GPS data (Figure 4b) exhibit uplift for most of the coastal stations with a maximum of 9.0 ± 1.4 mm/year (PB05) at sGPS stations near Mejillones peninsula at 23°S latitude and a maximum of 5.9 ± 2.1 mm/year (PSGA) at cGPS stations close to the epicenter of the Iquique-Pisagua earthquake 2014. Further inland, the vertical displacements show a more inhomogeneous deformation pattern with subsidence rates of less than 2 mm/year south of 22°S.

3.2. Model Results

The weights for the model approach of 50 cGPS and 51 sGPS stations are defined as the square of the inverse error. Given the inhomogeneous distribution of cGPS and sGPS stations, we additionally tested different weighting ratios $w = w_{sGPS}/w_{cGPS}$ between campaign and continuous data by performing a least rms error analysis (Cavalié et al., 2013). A weighting ratio of $w = 2.5$ generates the best data fit (Figure S13a). Based on a similar approach, we increased the uncertainty (i.e., decreased the weights) of our vertical GPS

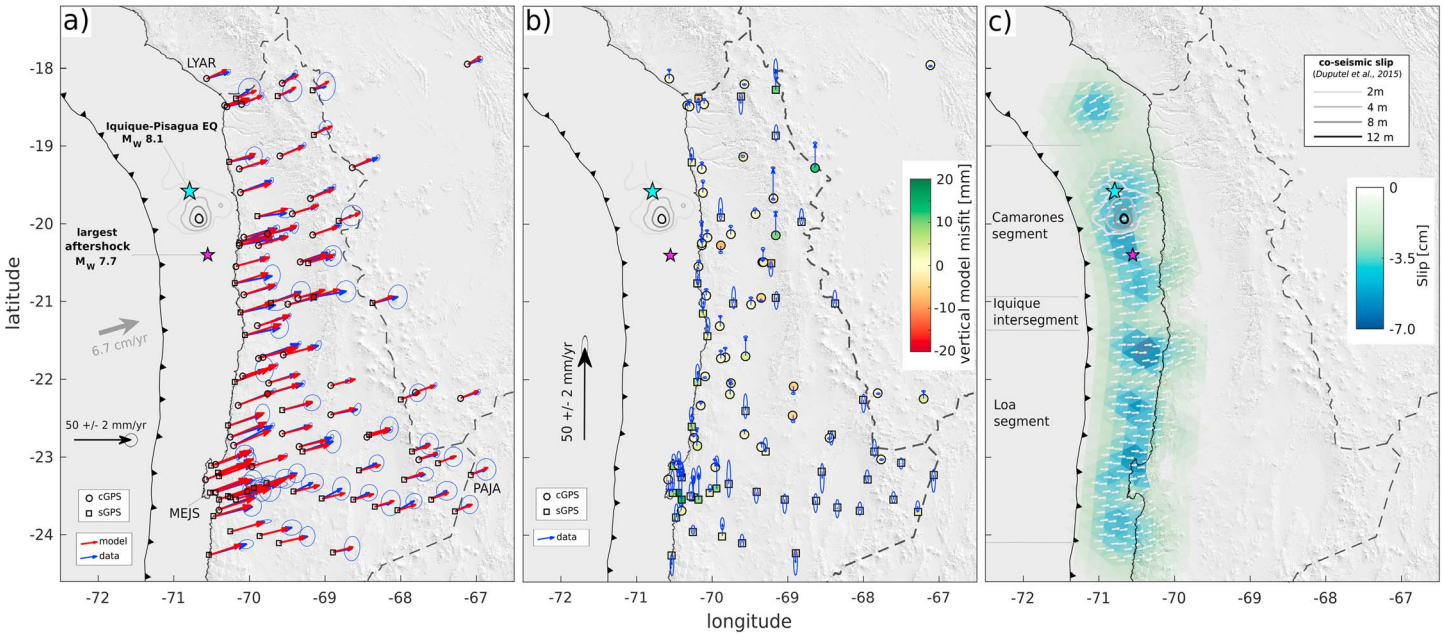

Figure 4. (a) Modeled (red) and observed (blue) Global Positioning System (GPS) displacements with 1-sigma uncertainties plotted in a stable South America reference frame, (b) corresponding vertical GPS observations (blue) with corresponding misfit indicated in colors (data minus model), and (c) modeled interseismic backslip on triangular fault patches on the subduction interface (white arrows indicate rake). Other features represent the coast line (solid line), the fault trench (solid line with triangles), political boundaries (dashed lines), and the coseismic slip model and aftershock location (Duputel et al., 2015). Inferred segment boundaries are marked with gray lines following the nomenclature of Métois et al, (2016). cGPS = continuous Global Positioning System; sGPS = survey-mode Global Positioning System.

components by a factor of 5 for cGPS and a factor of 10 for sGPS data (Figure S13b). The different weighting is necessary as in general, GPS data are more sensitive to horizontal motion and the vertical instrumental error might be underrepresented, especially for episodic GPS data acquisitions. Our interseismic backslip model locates the Euler pole representing the motion of the Andean sliver in central Ecuador (1.20°S, 77.31°W + 0.30°/Myr^{-1}). Amplitudes and azimuths of the resulting sliver motion are in agreement with Métois et al. (2013; 54.5°S, 37.5°W, −0.15°/Myr^{-1}), whose model was based on a different station network (Figure S14). However, the Euler pole of Métois et al. (2013) is located to the south of Chile, thus opposite of our pole, suggesting smaller sliver motion southward, where the active eastern front is lacking. In our case, the sliver rotation would be anticlockwise with a main NNE component of ground motion, which is in agreement with the preferred convergence direction in Northern Chile. The shortening of the Andean sliver accounts for 12–14 mm/year of the measured ground motion, which is consistent with other studies (e.g., Brooks et al., 2011; Métois et al., 2013). This rate corresponds to about 19% of the total convergence rate, which hence has to be reduced from 67 mm/year (Angermann et al., 1999) to 54 mm/year in Northern Chile for modeling if only data from the Chilean forearc are considered (Figure 4a). The backslip model yields an estimate for the degree of coupling of the plate interface in the decade before the Iquique-Pisagua earthquake. The coupling degree can easily be inferred from the slip rate: the higher the rate of backslip, the higher the degree of coupling. Coupling maps (e.g., Li et al., 2015; Métois et al., 2016) are given in ratios between 0 and 1, with 0 referring to freely slipping fault patches and implying that the interface moves with the full rate of the subducting Nazca Plate (54 mm/year after removal of 13 mm/year of sliver motion). Slip is generally considered as interface motion toward the trench and assumed to be positive. Therefore, backslip is directed away from the trench and assumed to be negative (Savage, 1983). Similar to previous plate interface coupling studies in Northern Chile (e.g., Chlieh et al., 2011; Li et al., 2015; Métois et al., 2016), our interseismic backslip model demonstrates a heterogeneous coupling distribution ranging from almost free slipping to full coupling of the plates with rates of up to 61 mm/year effectively realistic (Figure 4c). The backslip pattern in Northern Chile exhibits several highly coupled patches with rates >50 mm/year along the Chilean coastline at an intermediate depth of 30 to 40 km. These patches are separated from each other by low coupling areas of backslip rates less than 30 mm/year.

Most prominently, the central segment between 19.3 and 21°S latitude referred to as the Camarones segment (Figure 4c), where the Iquique-Pisagua earthquake ruptured, is clearly separated by lowly coupled zones to the north and south. The low coupling corridor at 21°S is referred to as Iquique low coupling zone (or Iquique interseismic segment) and was confirmed by others with slightly different extents (e.g., Li et al., 2015; Métois et al., 2016). Our interseismic backslip model generally compares well to previous coupling maps that detect highest coupling rates at a depth range of 20–40 km (e.g., Béjar-Pizarro et al., 2013; Chlieh et al., 2011; Li et al., 2015; Métois et al., 2016). But in contrast to these maps, our results show very low backslip rates at shallower depths $<$15 km, which could be explained by a lack of sensitivity in this depth range.

For sensitivity analysis, we perform a checkerboard test, in which we generate rectangular slip and backslip patches of size ~80 × 80 km in a checkerboard pattern of ±1 m slip on our interface geometry. This interface slip is forward modeled to yield ground deformation for our GPS network and inverted again. Inversion results can then be compared to the checkerboard geometry. The interseismic model is generally well resolved south of 19°S and in a depth range below 20 km and is less sensitive for the very north of our study area and the shallow interface parts (Figure S15b). Overall, we fit the GPS observations very well with a rms misfit of only 1.8 mm/year in horizontal direction (Figure S16a) and 1.7 mm/year in vertical direction (Figure S17a). In the north of the GPS network, the Euler rotation seems somewhat overpredicted, which causes a slightly underpredicted backslip rate. Our model fit the vertical data generally well, with a few exceptions at sGPS coastal stations to the south (Figures 4b and S18a).

4. Postseismic Period

4.1. Constraining Static GPS Displacements

We used the Euler pole obtained from the interseismic model (section 3.2) to correct the postseismic data for the sliver motion. Unlike for the estimation of the interseismic rates, where we extracted linear rates, we extracted static displacements for the three consecutive intervals, Periods 1–3, directly from the GPS time series (Tables S7–S12). Outlier detection and calculation of individual uncertainties for cGPS in the postseismic stage is the same as in section 3.1. For sGPS data, we increased the instrumental error by adding the overall rms position error of all (usually 3–5) daily solutions of one campaign. To further account for the instrument setup error, we lowered the relative weights for sGPS data with respect to cGPS data in the inversion (details in section 4.2). From the postseismic static displacements, we subtracted the viscoelastic response signal determined by the independent viscous model (section 2.3) in all three periods to account for the postseismic mantle relaxation (Tables S7, S9, and S11 and Figure S19). We still allow backslip to occur to assess possible rate changes on the interface in adjoining segments of the ruptured Camarones segment. Additionally, we subtracted the interseismic backslip rates, assuming that they are constant in time (Table S13) to account for relocking and extract the afterslip signal. For stations that were not active before 2014, we predicted an average relocking velocity based on our interseismic slip model (Figure 4c).

In Period 1 (days 2–16), stations north of 21°S exhibit trenchward (WSW) motion of up to 46.0 ± 1.2 mm some 80 km southeast of the inferred maximum slip (station CGTC, Figure 5a and Table S7). This motion is oriented opposite to the interseismic ground displacement direction prior to the event. Stations south of 21°S remain more or less unaffected by this early postseismic motion and continue to move in the direction of plate convergence (2.3 ± 1.2 mm, PB03). The latitudinal displacement gradient is not symmetric around the peak slip region at 20°S: from there, the displacement decrease is ~14 mm within the first 100 km northward, whereas the decrease is faster, ~18 mm within the first 100 km, southward (Figure 5a). The vertical GPS data (Figure 5d) exhibit subsidence of all stations, with a maximum of 25.4 ± 2.3 mm (PSGA) at stations that are located close to the epicenter of the aftershock.

In Period 2 (days 17–334), the displacement pattern slightly changes: the maximum trenchward displacement has shifted about 50 km away from the coast and reaches 58.9 ± 2.2 mm at cGPS station PB11 (Figure 5b and Table S9). The asymmetric surface deformation pattern becomes more prominent, with a displacement decrease of ~34 mm northward and a decrease of ~46 mm southward within the first 100 km (Figure 5b). Moreover, the abrupt displacement sign change of stations from north to south of 21°S is more obvious. GPS station PB01 is the southernmost station that moves toward the rupture zone (11.8 ± 1.3 mm), whereas GPS station PB02, located only ~40 km south of PB01, moves opposite (16.7 ± 1.3 mm) before the relocking signal is subtracted. All stations south of 21°S move collinear with the plate convergence vector

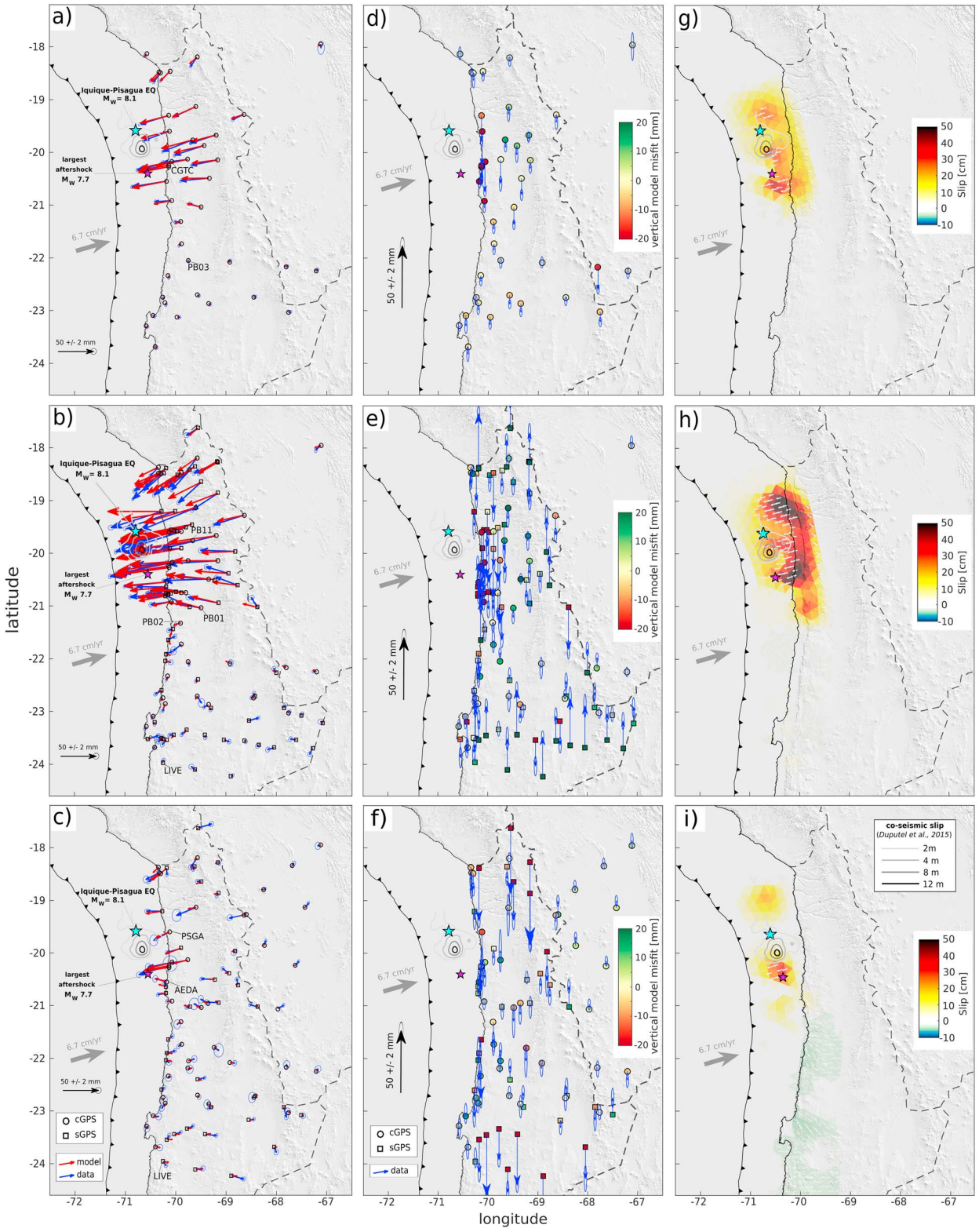

Figure 5. (a–c) Predicted displacements (red) in comparison to the Global Positioning System observations (blue) with 1-sigma uncertainties, after subtracting the relocking signal (average interseismic rate) and the viscoelastic response for (a) 2–16 days (Period 1), (b) 17–334 days (Period 2), and c) 335–717 days (Period 3) after the mainshock. (d–f) Vertical GPS observations (blue) and color-coded model residuals for the corresponding postseismic Periods 1–3. (g–i) Predicted post-seismic afterslip on the plate interface during the corresponding postseismic Periods 1–3. For other features see Figure 4. cGPS = continuous Global Positioning System; sGPS = survey-mode Global Positioning System.

with a maximum of 28.9 ± 2.0 mm at station LIVE, which nearly corresponds to its interseismic rate of 31.7 ± 5.5 mm for 1 year. The vertical GPS data (Figure 5e) close to the main rupture exhibit subsidence of up to 23.9 ± 2.6 mm (PSGA), whereas stations toward the south of the epicenter region show uplift of 33.0 ± 2.8 mm (PRO2). This spatial sign change may represent the hinge line of postseismic uplift to subsidence at a latitudinal range of ~21–22°S. In general, the vertical displacement pattern seems more coherent for cGPS than sGPS observations. Uplift rates of sGPS data toward the south may be systematically overestimated compared to cGPS rates.

During Period 3 (days 335–717), most of the stations north of 21°S have significantly reduced their trenchward motion and relocking dominates over the afterslip component of the signal. For example, the cGPS station (PSGA) closest to the mainshock exhibits a displacement of 5.0 ± 3.7 mm toward ENE before subtracting relocking (Figure 5c and Table S11). Stations south of 20.5°S feature ENE displacement that increases southward from 15.4 ± 2.2 mm (AEDA) to 35.8 ± 1.4 mm (LIVE) before subtracting relocking velocity (Figure 5c). The vertical GPS data (Figure 5f) is relatively inhomogeneous. Coastal stations close to the main rupture still mostly exhibit subsidence with a maximum of −19.3 ± 6.1 mm (PSGA), whereas few stations south of 21°S (8.5 ± 2.2, PB03) and in Bolivia (3.7 ± 1.7, BMWS) experience uplift. The sGPS rates seem less coherent with generally higher subsidence rates toward the south (−10.3 ± 3.0 mm, PRO3) compared to cGPS rates (−6.6 ± 3.1 mm, JRGN).

If we analyze the temporal evolution of displacement by using a moving window of 30 days, we illustrate for how long each GPS station was affected by the Iquique-Pisagua earthquake (Figure 6). As reported before, stations south of 21°S seem not at all affected by the mainshock. Stations south of PB01 have an eastward trend collinear with the plate convergence over all investigated periods. But just 40 km north, at 21°S, the adjacent stations CRSC, CLLA, and PB01 are clearly affected by coseismic and postseismic response to the mainshock (Figure 6). The majority of GPS stations north of 21°S turn their sense of motion from trenchward to landward after about 1 year, thus slowly converging to interseismic relocking. This turnover of ground displacement motion back to interseismic relocking with surface motion collinear to the plate convergence vector is almost completed after 2 years. After April 2016, westward directed motion induced by afterslip is dominated by eastward directed motion induced by relocking and we assume interface afterslip to become negligible with less than 5 cm/year 2 years after the Iquique-Pisagua event.

4.2. Model Results

The slip models of the different postseismic stages yield a more detailed picture of the temporal evolution of afterslip (Figures 5g–5i). For the postseismic models, we first calculated the data weights based on GPS uncertainties and then introduced the weighting factor $w = w_{sGPS}/w_{cGPS}$ (Figure S13a), similar as for the interseismic model (section 3.2). Period 1 only contains cGPS data (42 stations), but for Period 2 (38 cGPS and 64 sGPS stations, $w = 2.0$) and Period 3 (33 cGPS and 43 sGPS stations, $w = 1.5$), we defined different relative weights to account for a difference in spatial distribution of cGPS and sGPS stations. Similar to the postseismic modeling approach, we increased the uncertainty of the vertical GPS component by a factor of 5 for cGPS and 10 for sGPS data to more realistically represent the vertical data error (Figures S13c and S13d).

While subtracting averaged interseismic rates from postseismic data before inverting for postseismic slip, we assume that the relocking rates remain constant before and after the Iquique-Pisagua event 2014. This may lead to an overestimation of afterslip rates and also the viscoelastic relaxation component of the signal, if interseismic loading signal does not resemble prevailing backslip during the postseismic period.

In Period 1, afterslip with a magnitude of 15–25 cm surrounds the rupture area of the Iquique-Pisagua earthquake downdip at ~30–35-km depth (Figure 5g). Maximum slip of up to 38 cm occurs 50 km south of the mainshock at ~30 km depth, near the epicenter of the largest aftershock. In a latitudinal range of 20.7–21°S, our model indicates a transition from highest slip rates to backslip-dominated interface motion. We think that this pattern is caused by the sharp latitudinal sign change of displacement and might be linked to a seismotectonic barrier at 21°S. This sharp transition moreover suggests that stations south of this zone are not affected by afterslip (Figure 5g).

In Period 2, afterslip occurs downdip of the main rupture at 30–50-km depth, surrounding the hypocenter and reaching peak values of 51 cm (Figure 5h). One-peak slip patch is located 50 km south of the epicenter, again at the location of the largest aftershock, and a second high afterslip patch appears 40–50 km to the

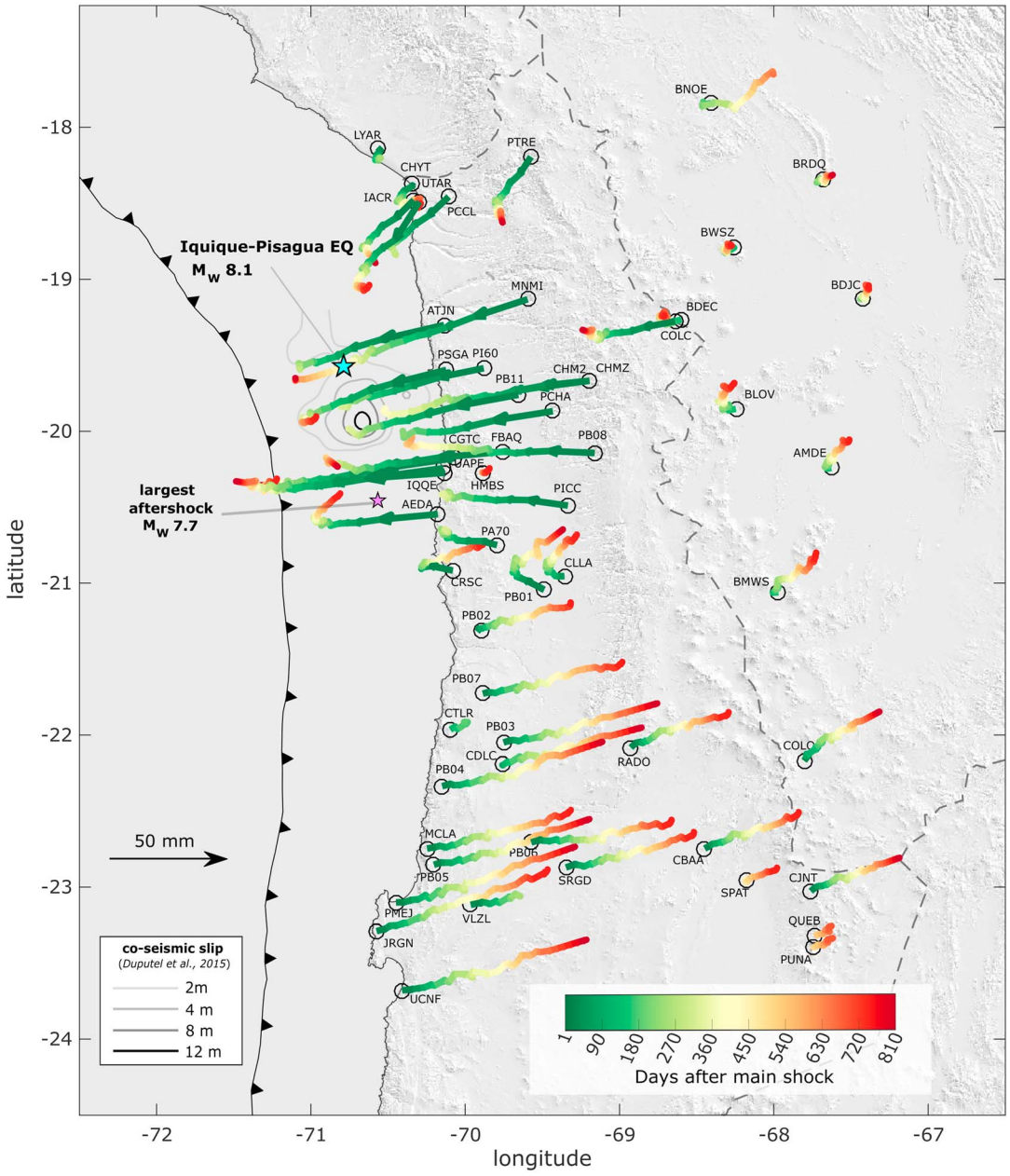

Figure 6. Postseismic ground displacement color coded by days after the mainshock (sampled every 30 days). For other features see Figure 4.

north of the main rupture at ~35–40-km depth. The updip area of our slip model exhibits significantly less slip, only 10 to 20 cm. The geometry of afterslip extent during the first year after the earthquake is surprisingly similar to the afterslip pattern of the first 2 weeks, except for the larger magnitudes. Afterslip in Period 2 involves deeper parts of the interface and is shifted ~20 km northward compared to Period 1 as visible at the aftershock peak slip. A relatively sharp transition from slip to backslip-dominated interface motion is again detected at 20.7–21°S. At this latitude, slip extends about ~40 km further south underneath the Chilean coast, thus at relatively poorly resolved, deeper parts of the interface. No difference to interseismic interface motion can be observed south of this latitudinal range as inferred by a lack of slip/backslip southward.

In Period 3, afterslip has significantly decreased and converges to 0 in the center of the inferred rupture zone of the Iquique-Pisagua mainshock (Figure 5i). This reflects the transition from an afterslip-dominated stress

regime to relocking as described by Wang et al. (2012). One isolated afterslip patch is located ~50 km north of the epicenter with 10–15-cm slip. Surprisingly, peak slip occurs consistently at the area of the largest aftershock 50 km south of the mainshock, with slip of 35 cm in Period 3. The spatial transition from afterslip at the Camarones segment to interseismic relocking at the southern Loa segment becomes more diffuse in Period 3 but is shifted northward compared to Period 2 (nomenclature from Métois et al., 2016). Most prominently, south of 21°S, we observe increasing backslip rates in an interface depth range of 40–60 km. After having subtracted averaged interseismic loading rates from our observations, we expect interface slip in adjoining seismotectonic segments that are not affected by afterslip to be close to 0. In contrast, backslip rates up to −2.5 cm south of 21°S indicate a coupling increase of the subduction interface in the second year after the megathrust event. Peak backslip rates are located at 45–50-km depth underneath Mejillones peninsula at ~23°S.

Overall, a cumulative peak afterslip of 89.0 + 1.2/−0.4 cm is observed within the first 2 years after the Iquique-Pisagua earthquake, occurring between 30 and 45 km depth and embracing the rupture area downdip (Figure S20). We estimated the error of the maximum slip using a simplified Monte-Carlo approach calculating the standard deviation of 50 inversions in which we added normally distributed noise to the GPS data (Figure S21). A sharp transition between afterslip to the north and backslip (increased interseismic coupling) to the south is observed in a latitudinal range of 21–21.5°S. Most interestingly, the pattern complements the high backslip pattern observed in the interseismic phase at these latitudes (Figure 4c).

The model resolution based on our checkerboard approach (section 3.2) for all three periods is generally good (Figures S15c and S15d). An exception is the southern part of Period 1, where we have rather poor resolution south of 23°S mainly due to the lack of GPS stations there as we only use cGPS data. But the expected afterslip area south of the mainshock epicenter, toward the largest aftershock, is well resolved below a depth of ~15 km. However, potential shallow afterslip above 15 km might not be resolvable with our model geometry.

The postseismic models fit the horizontal data of all three stages reasonably with a rms residual of 1.7 mm (Period 1), 4.2 mm (Period 2), and 2.4 mm (Period 3) (Figures S16b–S16d). The strongest horizontal misfit is observed in Period 2 at coastal stations close to the main rupture and to the north. Further tests have shown that the misfit cannot be significantly improved by changing model parameters (i.e., depth constraints or smoothing value). The overall direction of deviation is toward the south, implying a northward shifted model slip. One reason for the northward shift of slip could be the unfavorable spatial resolution of our model geometry that is poorly resolved at shallow parts of the interface as well as north of 19°S due to a lack of Peruvian GPS data. Thus, potential shallow afterslip may be shifted deeper and northward to better fit the observations. A more physical explanation for the deviation could involve rheologic inhomogeneity in the crust, which are not taken into account in our half-space model. The relatively high misfit and systematic underprediction of the southward displacement in Period 2 may be a consequence of our simplified model rheology. To better fit the data, a more complex geometry involving a three-dimensional model setup may be needed (e.g., Klein et al., 2016; Li et al., 2015). Another cause for local (point-wise) misfit of the GPS vectors as, for example, observed for stations VIRI or COLC in Period 3 could be upper crustal faulting, as has been observed in many parts of Northern Chile and Bolivia (e.g., Allmendinger & González, 2010; Lamb, 2000). González et al. (2015) even argued that the Iquique-Pisagua mainshock could have been triggered by a reactivated trench-oblique upper plate reverse fault (the M_w 6.7 foreshock on 16 March 2014). However, we do not observe a spatially coherent, long-wavelength misfit pattern in the far field as potentially caused by viscous relaxation (Wang et al., 2012). Thus, we believe that our model predictions for the viscoelastic component represent the amount of mantle relaxation contributing to the measured postseismic ground deformation signal well.

The vertical displacement predications fit the data worse than the horizontal predictions and exhibit a rms residual of 3.5 mm (Period 1), 5.2 mm (Period 2) and 2.0 mm (Period 3; Figures S17b–S17d). The model clearly fails to properly predict the highly complex vertical displacement and, again, a three-dimensional model would probably improve the fit, for example, by including a complex crustal structure that accounts for features like local low-viscosity channels (e.g., Klein et al., 2016; Figures 5d–5f and S18b–S18d). Another reason for the poorly vertical fit is the relatively large data uncertainty of the vertical data, particularly for episodic measurements that can be explained by the acquisition geometry allowing more sensitivity to

horizontal measurements. Another systematic overrepresentation of vertical data is apparent close to the rupture area of the mainshock, whereas the up component toward the south is clearly underrepresented. Nevertheless, our model is capable of resolving the hinge line between postseismic uplift and subsidence at coastal stations between 20 and 21°S in Periods 1 and 2. In Period 3, this hinge line may has shifted offshore.

5. Discussion

5.1. Spatial Correlation of Afterslip and Aftershocks

The afterslip pattern of the Iquique-Pisagua earthquake is comparable with the postseismic deformation of other megathrust events of the last decade. Similar to the 2005 Nias M_w 8.7 Sumatra event (Hsu et al., 2006) or the 2010 Maule M_w 8.8 Chile earthquake (Bedford et al., 2013), afterslip surrounds the region of maximum coseismic slip and occurs mostly in the downdip area of the rupture (Figures 5g–5i). To shed light on this and better understand the relation between afterslip and aftershocks, we analyzed the location of aftershocks of the first year after the earthquake. For this we utilized a recently compiled seismicity catalog from the IPOC permanent station network that covers the years 2007–2014 (Sippl et al., 2018). The catalog contains a total of 101 k events and has good spatial coverage of the Northern Chile-Southern Peru seismic gap, with a completeness magnitude of 2.7–2.9. Events were detected using the multistep procedure of phase picking and relocation outlined in Sippl et al. (2013), the last step of which is double-difference relocation using event pair cross correlations.

In the first 2 weeks after the Iquique-Pisagua mainshock, modeled peak afterslip occurs north and southeast of the rupture area (Figure 5g), near the epicenter of the large aftershock, where interseismic backslip (coupling) is highest (Figure 4c). This suggests that in the first few days after the mainshock, afterslip neutralizes incomplete coseismic stress drop, as it was also reported after the 2010 Maule earthquake (Bedford et al., 2013). In the same period, aftershocks mostly occur in the rupture area. The distribution of aftershocks in the first days following the mainshock may thus be controlled by the redistribution of stress during the coseismic phase (Figure 7a; e.g., King et al., 1994).

The early stage of afterslip is characterized by the presence of both, normal and thrust faulting earthquakes, but after 2 weeks only thrust mechanisms dominate in the aftershock sequence. This may reflect a minor temporal change of the compressional axis of about 6° and premegathrust stress conditions were restored a few weeks later (Cesca et al., 2016). Aftershock locations in the first year after the mainshock until the end of 2014 seem to flank the highest coseismic rupture areas (slip above 8 m) but also border the regions of high afterslip (Figure 7b). In a band-like geometry, aftershocks separate the northern peak afterslip patch from the southern one. Modeled afterslip mostly occurs deeper than ~35 km and reaches the assumed transition zone from (brittle) crust to the hydrated mantle wedge (e.g., Bloch et al., 2014). Given the clear spatial correlation between peak afterslip and the absence of aftershocks in Period 2 (Figure 7b), we infer that postseismic stress release is mostly transferred from aseismic (rate-strenghtening) peak afterslip areas to adjacent intermediate afterslip regions close to the coseismic rupture zone. The updip area exhibits relatively low afterslip, which agrees with the observation of the low degree of interseismic coupling in the shallower parts of the interface, where slip deficit is assumed to be almost 0 (Li et al., 2015). This possibly indicates interseismic creep on the updip portion of the plate interface. On the other hand, our checkerboard tests (Figure S15) show that the shallow parts of the interface are poorly resolved, and the relatively intense updip seismic activity indicates rate-weakening behavior. North of 19°S, the seismicity in the downdip high afterslip area decays rapidly (Figure 7b). Thus, the aseismic area in the north seems to release stress while creeping, which potentially reflects a transient increase of pore fluid pressure (Kodaira et al., 2004). Moreover, this region spatially correlates with low coupling in shallow to intermediate crustal depths of 10–30 km (Figure 4c), probably indicating the border to another seismotectonic segment (Li et al., 2015; Métois et al., 2013). This could also explain the relatively low GPS displacement rates north of 19°S in the interseismic (Figure 4a) and postseismic period (Figures 5g–5i) that are probably caused by a low-coupled segment to the north that is separated from the Camarones segment where the mainshock ruptured. Moreover, the distance to the trench increases toward the north, which also contributes to a slowing down of the GPS velocities there.

South of 21°S, the high-afterslip zone also exhibits a significant decrease of seismicity. The rupture area of the mainshock terminates near a low coupling zone (Iquique intersegment, Métois et al., 2013) at 20°S

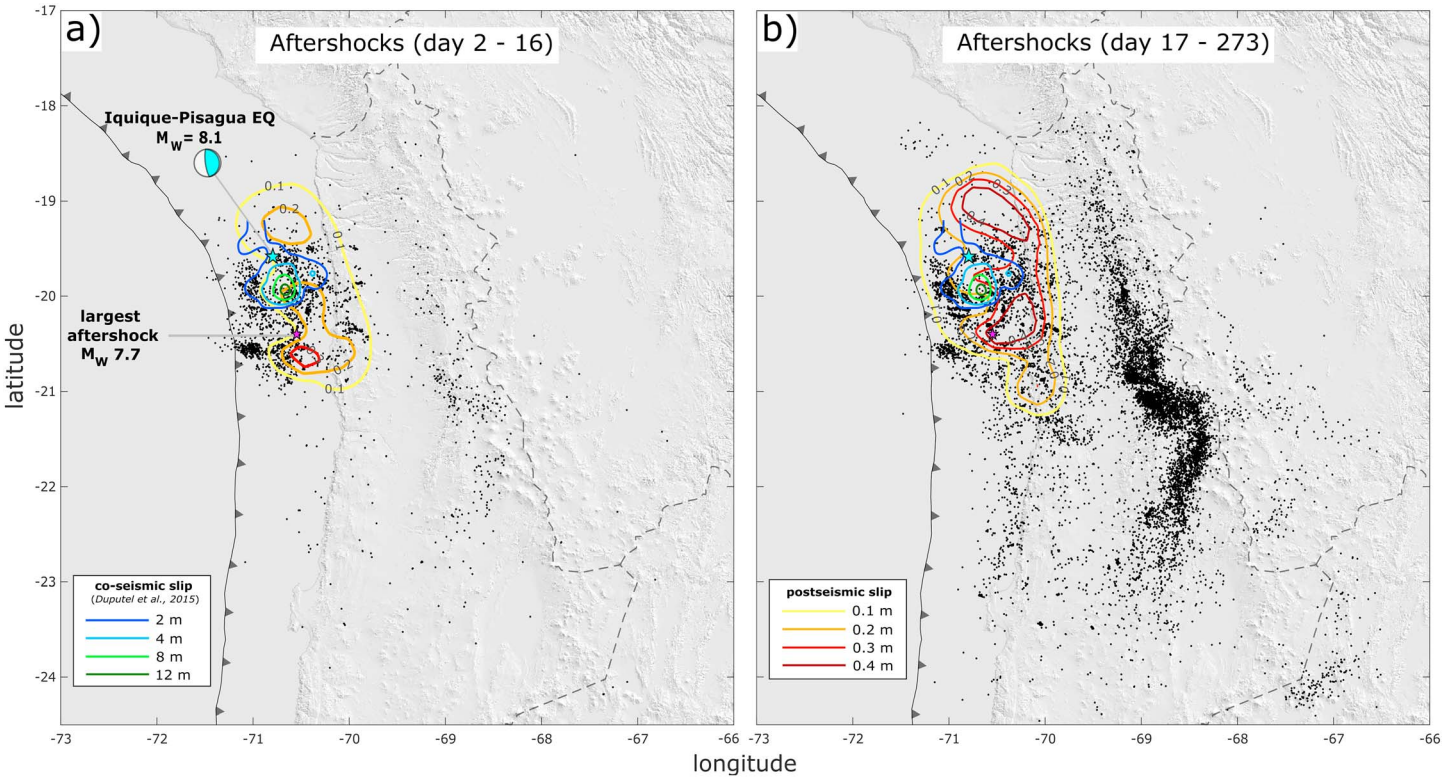

Figure 7. Aftershock distribution (Sippl et al., 2018) during (a) Period 1 and (b) Period 2 in comparison to coseismic slip (blue/green isolines) (Duputel et al., 2015) and modeled afterslip (yellow/red isolines) in the respective intervals. Each coseismic slip represents an increment of 2 m, each afterslip contour an increment of 0.1 m. Note that in (b) only aftershocks until the end of 2014 are included. For other features see Figure 4.

(Duputel et al., 2015; Ruiz et al., 2014; Schurr et al., 2014), but afterslip extends further south across to 21°S, probably due to the effects of the large aftershock (Figure 8a). Low coupling zones are assumed to behave in a rate-strengthening way, increasing their frictional strength, thus decreasing the likelihood of slip propagation (e.g., Scholz, 1998). But the afterslip also affects this interseismically low coupled zone and terminates abruptly at ~21.2°S (Figure 8a), where the seismicity likewise decreases sharply. Similar to above, the coupling differences may reflect a seismotectonic barrier.

In Period 2, a N-S oriented, left-stepping, band-like structure of seismicity becomes more prominent at 80–120 km depth and 250–300 km east of the trench (Figure 7b) and is most densely populated between 20° and 22.5°S. The spatial extent of this band correlates neither with the shallow seismicity described above nor with the coseismic or postseismic slip on the plate interface. The occurrence of this intermediate-depth seismicity is most likely caused by the metamorphic dehydration of the oceanic lithosphere effecting hydraulic embrittlement due to the release of fluids (Bloch et al., 2014; Rietbrock & Waldhauser, 2004; Yoon et al., 2009). The observed kink in the seismic band spatially correlates with the southern limit of the afterslip zone at 21°S. South of the kink, the dehydration-related seismicity occurs slightly deeper, which probably reflects heterogeneity in the subducting oceanic plate (e.g., Geersen et al., 2015) or crustal rheology.

We additionally generated a simple Coulomb failure stress (ΔCFS) change model based on our viscoelastic model geometry and the coseismic shear (σ_s) and normal stress (σ_n) changes on the interface:

$$\Delta\mathrm{CFS} = \sigma_s - \sigma_n \cdot \mu \tag{3}$$

with $\mu = 0.1$ as the coefficient of friction (Lamb, 2006). In our model, positive ΔCFS outlines the main rupture area updip and downdip (Figure 8b), indicating that those interface regions were brought closer to failure and are more prone to aftershocks during the postseismic stage. For the updip part, where we lack model resolution, aftershock locations are in good spatial agreement with positive ΔCFS. For the downdip area, aftershocks occur in both, positively and negatively loaded ΔCFS regions. The negative ΔCFS of up to −4 Mpa spatially coincides with the high coseismic slip regions of the rupture area of the Iquique-Pisagua

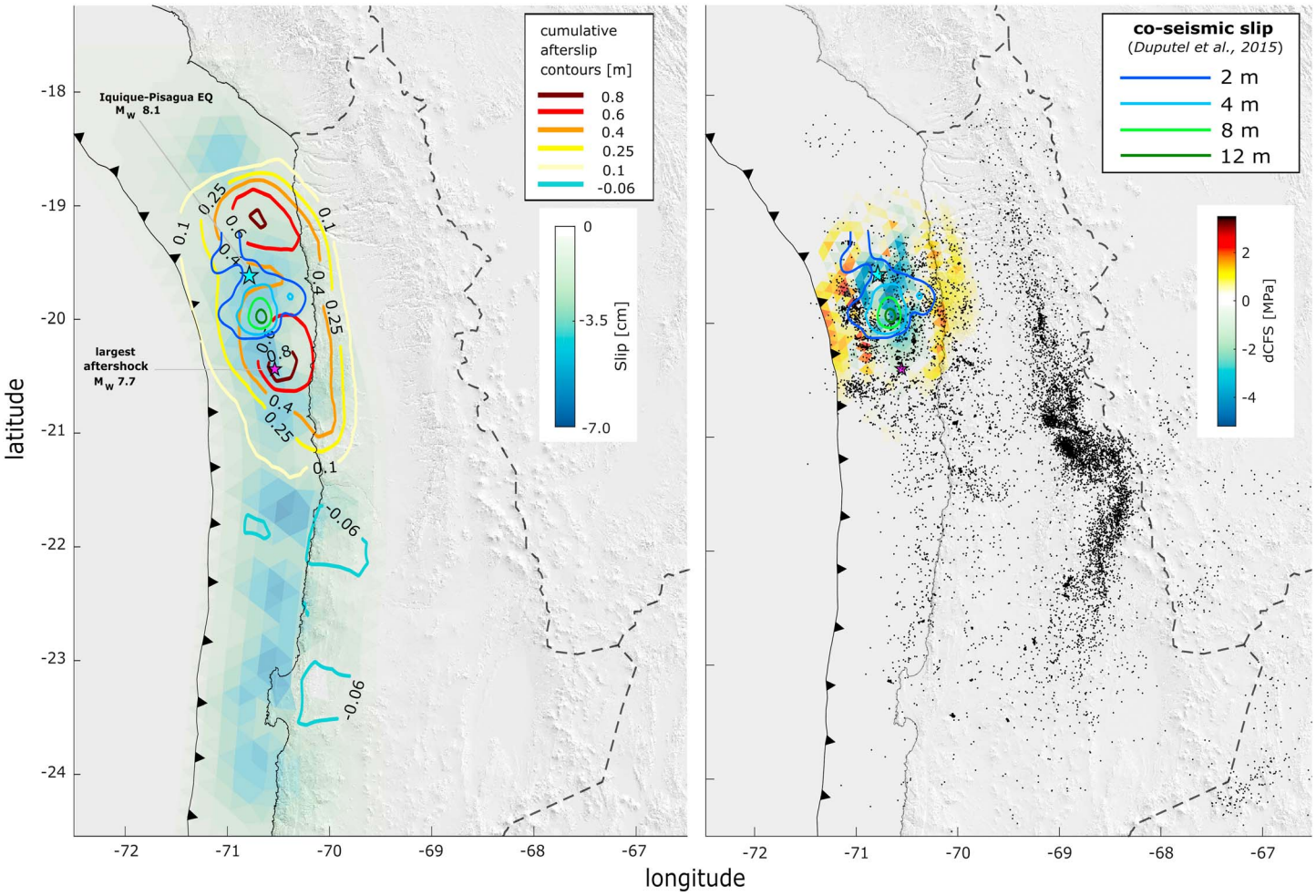

Figure 8. (a) Comparison of interseismic backslip, coseismic slip (Duputel et al., 2015) and cumulative afterslip (see also Figure S20). (b) Comparison of coseismic slip, estimated Coulomb failure stress changes based on slip model of Schurr et al. (2014), and aftershocks from April to December 2014 (Sippl et al., 2018). For other features see Figure 4.

mainshock, where significantly fewer aftershocks occur. The largest aftershock is located at the southern edge of the negative ΔCFS region. This may be associated to premainshock stress conditions and potentially reflects interseismic stress buildup preceding the mainshock, for example, due to the foreshock on 16 March 2014 (e.g., González et al., 2015).

5.2. Seismotectonic Barrier at 21°S

In all our observations, we find that the region at 21°S acts as a barrier or apparent discontinuity of physical properties. Throughout the whole investigated period, the GPS stations south of 21°S move permanently in the interseismic ENE direction, indicating that the plate interface remains strongly coupled (Figures 4a, 5a–5c, and 8a). In the postseismic stage, we observe sharp GPS rate changes near 21°S that coincide with the southern termination of the narrow, low-coupled zone (Iquique low coupling zone) (Figure 8a; Métois et al., 2016). Afterslip intrudes into this possibly rate-strengthening zone south of 21°S, which we interpret as postseismic stress transfer into a very heterogeneous subduction interface (e.g., Kaneko et al., 2010; Marone et al., 1991) at the border to a region undergoing stress buildup (south of 21°S). This transition zone also shows peak seismicity at the upper plate both before and after the 2014 earthquake (Meng et al., 2015; Figure 7b) and potentially indicates a seismotectonic barrier, which is less coupled with respect to adjacent segments. The barrier may thus be a consequence of mechanical variations in the coupling between the interface and the upper plate. Geersen et al. (2015) attribute the heterogeneous coupling to seamounts on the subducting plate that prevented the Iquique-Pisagua rupture to migrate southward. According to them, the so-called Iquique

Ridge at 19.5–21°S (Figure 1) favors aseismic conditions with smaller earthquakes and creep rather than large ruptures due to extensive fracturing at the plate boundary (Geersen et al., 2015; Wang & Bilek, 2011). Another explanation for the presence of the barrier could be a postulated abrupt change of slab dip at ~21°S, interpreted as slab bending in recent studies (e.g., León-ríos et al., 2016). In the numerical model of Kaneko et al. (2010), two rate-weakening zones were separated by a narrow rate-strengthening block. This is comparable to the tectonic setting of our study, where two highly coupled zones are separated by the narrow Iquique low coupling zone at 21°S (Figure 8a). Whenever one of the rate-weakening zones ruptured individually in this experiment, stress was transferred to the opposite zone that, in turn, was brought closer to failure than expected from the original recurrence interval (Kaneko et al., 2010). These results focus our attention to the southern Loa segment at 21–23°S.

However, the origin of the seismotectonic barrier might also be related to the upper plate rather than to the plate interface. Loveless et al. (2009) reported that the preferred orientation of surface cracks north and south of 21°S changes from NNW to NE, indicating two distinct stress regimes in the upper crust. This zone is also the southern limit of E-W trending faults (Figure 1) responsible for along-strike shortening of the Coastal Cordillera (Allmendinger & González, 2010; Allmendinger et al., 2005). These authors have related this kinematic observation to the location of the symmetry axis of the Andean orocline (Gephart, 1994; Figure 1) as well as of the Benioff Zone. This finding is also supported by numerical analysis and analog simulation in Boutelier and Oncken (2010) and Boutelier et al. (2014), both of which suggest that bending in conjunction with specific plate interface properties have a key role in the kinematic response. The seismotectonic barrier correlates spatially with the boundary between a strongly faulted upper plate domain in the North and an unfaulted upper plate in the South (Allmendinger & González, 2010). From these observations together with the observed sharp gradient in surface motion, we additionally speculate that there could be an associated strength change of the forearc crust.

The seismotectonic barrier at 21°S potentially prevented the Northern Chile-Southern Peru seismic gap region to rupture in a single event as in the 1877 Iquique M_w 8.6 earthquake (e.g., Comte & Pardo, 1991). Although there is also some discordance about the actual size of the 1877 event (Métois et al., 2013), this earthquake was certainly larger than the 2014 event and either extended the barrier, or the barrier was only formed in the postseismic and interseismic stage following the 1877 event. The 2014 earthquake could only partially release the slip deficit accumulated since 1877 (Métois et al., 2013; Schurr et al., 2014). Consequently, for further analysis the seismic gap region should be split into two parts separated by the seismotectonic barrier at 21°S. Moreover, our results suggest that the seismotectonic behavior may be more strongly affected by upper plate strength variations along the Chilean margin than previously surmised.

5.3. GPS Rate Change South of 21°S

GPS rates south of 21°S reflect the crustal response to the occurrence of the 2014 earthquake at this unbroken adjacent segment. Here we find a significant rate change of up to 10 mm/year over different postseismic periods after the Iquique-Pisagua earthquake. To illustrate this, we extracted the linear trend from the time series of Periods 2 and 3 as described in section 2.2 and calculated the rate changes with respect to the interseismic rates observed before the earthquake (Figure 9). In the first year after the mainshock, stations south of 21°S latitude experienced a rate decrease compared to the preearthquake rates, whereas in the second year those stations (consistently sGPS and cGPS) show a rate increase (Figure 9). This rate increase may not be dependent on the distance between station and trench as maximum acceleration is observed at inland stations at distances of 130 to 170 km away from the trench and not at coastal stations that are closer to the trench. We interpret this change of behavior between the first and the second year following the Iquique-Pisagua earthquake as response to decreasing afterslip rates and the dominant effect of interseismic deformation at the southern Loa segment. Hence, the rate decrease in the first year could be explained by the interaction of (1) far-field afterslip on the interface and (2) viscoelastic relaxation. Both mechanisms cause GPS stations to move toward the rupture zone, opposite to the ongoing interseismic coupling locking (Bedford et al., 2016; Wang et al., 2012). Therefore, the observed rate decrease in the first year could be the consequence of relaxation processes. This confirms that the viscoelastic relaxation decays fast, being more dominant in the first year after the event. But what causes the rate increase in the second year after the earthquake, which is comparable to what was reported from adjoining segments of the 2003 Tokachi-Oki M_w 8.0, Japan earthquake (Heki & Mitsui, 2013)? One explanation may be given by recent studies of Melnick et al. (2017) and Klein et al. (2016)

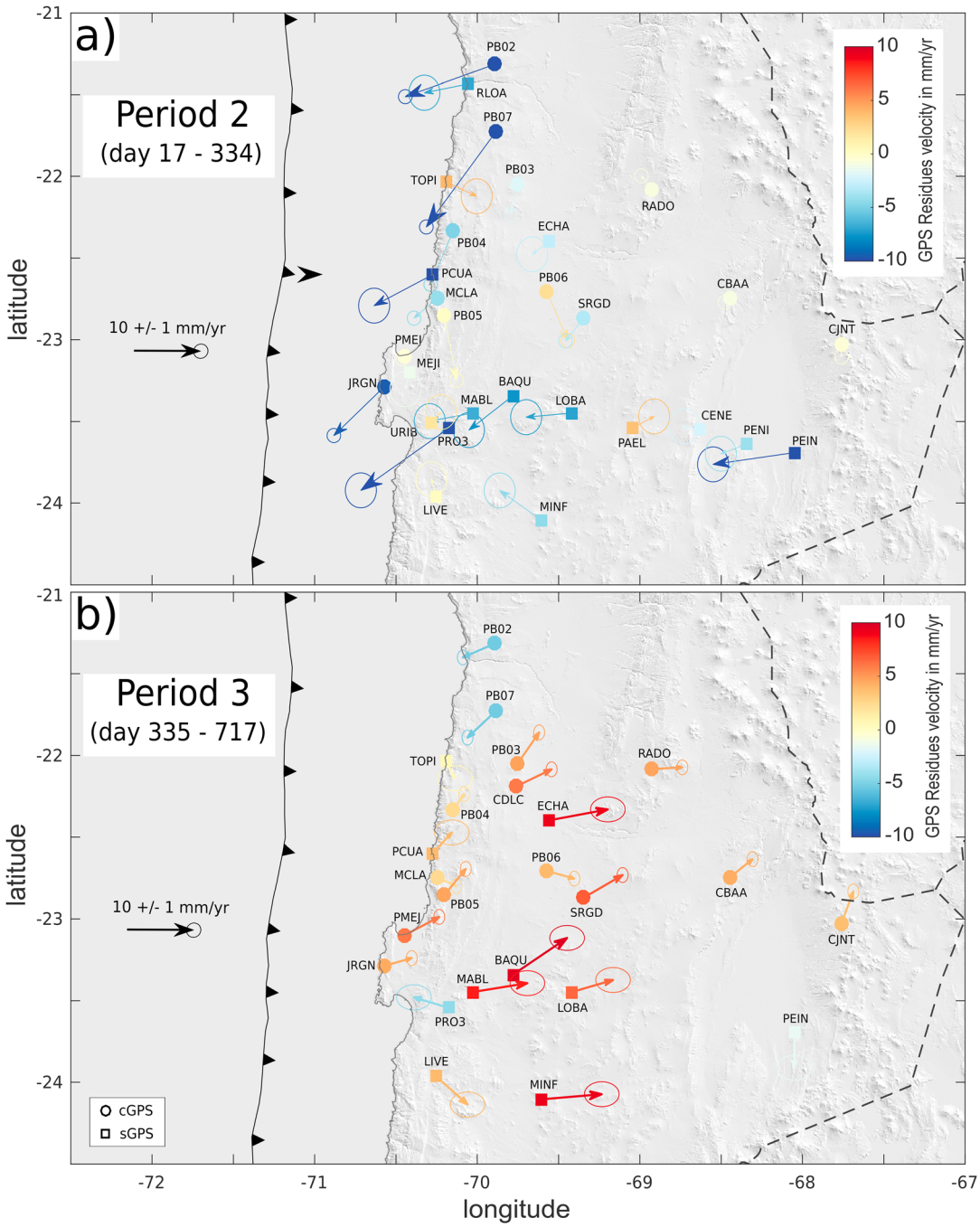

Figure 9. Rate changes during (a) Period 2 and (b) Period 3 after the Iquique-Pisagua earthquake with respect to the pre-event displacement rates. The vectors are color coded by the amplitude of the rate change; the symbols mark continuous (circle) and campaign (square) GPS rates. GPS = Global Positioning System.

that documented GPS rate increase after the 2010 Maule earthquake at the adjacent unbroken segments. Likewise, we propose that the observed rate increase south of 21°S can be an effect of continental-scale, viscoelastic mantle relaxation (Klein et al., 2016) that induces an increase of fault shear stresses more than 200 km away from the rupture zone. The increase of interseismic rates can also be mechanically related to the elastic flexural bending response of both plate segments to the uncoupling after a large earthquake in one of the segments. This uncoupling may increase the interseismic stress accumulation at adjacent clamped (locked) segments (Melnick et al., 2017). Our models confirm these temporal variations of

interseismic rate after a large earthquake and suggest a significant increase in backslip rate of up to 10 mm/year (Figure 9) and thus increased interface coupling in the second year after the earthquake (Figure 5i). The observation that maximum rate increase occurs not at coastal stations, but 40 to 80 km inland potentially reflects downdip changes of interface coupling deeper than 40 km at the downdip limit of the seismogenic zone. Similar to the potential triggering of the 2015 Illapel M_w 8.2 earthquake (Tilmann et al., 2016) by the 2010 Maule M_w 8.8 event as bimodal megathrust occurrence (Klein et al., 2016; Melnick et al., 2017), we suggest that the Iquique-Pisagua event can bring the Loa segment closer to failure due to increased shear stress at the downdip limitation of the fault.

Another, more speculative hypothesis locates the source of surface displacement rate increase to the upper crust, particularly if we assume that our elastic models somewhat overestimate the coupling degree. This would be the case, if we underestimate the viscoelastic relaxation or the interseismic loading prior to the earthquake. Given the complexity of our time series that cover the full seismic cycle including two major earthquakes (the 2005 Tarapacá and 2007 Tocopilla event) that affect velocities in our pre-Iquique-Pisagua earthquake interval, our extracted loading rates may be underestimated. In this case, we should detect a time-dependent increase of upper crust weakening and the current slip deficit would be released aseismically. Another realistic explanation for coupling increase in our models involves our simplified model rheology with a homogeneous, linear Maxwell viscosity that does not account for complex rheologic features like low-viscosity wedges (e.g., Klein et al., 2016). However, the consistency and uniformity of the change of the interseismic velocity field, observed in both, sGPS and cGPS data, suggest an increase of shortening rate at the Loa segment independent of our modeling strategy. Longer postseismic time series will provide valuable data to our findings and to further investigate the temporal variations of coupling degree.

6. Conclusion

Based on 152 GPS time series, we have derived an interseismic backslip model of the (former) Northern Chile-Southern Peru seismic gap and three consecutive postseismic models documenting 2 years of afterslip motion following the 2014 M_w 8.1 Iquique-Pisagua earthquake. Prior to the earthquake, we find a heterogeneously locked plate interface with two highly coupled patches in the central part of the gap that are separated by a narrow, low-coupling zone at 21°S (Iquique low coupling zone), probably acting as a seismotectonic barrier. Consequently, the rupture area of the 1877 M_w 8.6 Iquique earthquake should be analyzed as two distinct patches.

The postseismic models exhibit peak afterslip at the location of the largest aftershock and show a relatively sharp gradient from trenchward to landward motion at ~21°S latitude. Based on this strong displacement gradient as well as mapped changes in upper plate faulting and crack orientations, we speculate that crustal strength heterogeneity may contribute to cause this seismotectonic barrier.

Cumulative afterslip reaches 89.0 + 1.2/−0.4 cm, outlines the main rupture area downdip and dissolves after 2 years. The Loa segment south of 21°S is unaffected by afterslip but yields a significant rate increase toward interseismic ground displacement direction of up to 10 mm/year in the second year following the earthquake. We interpret this as an increase in downdip interface coupling due to shear stress increase as a consequence of regionally induced deformation (viscoelastic and/or elastic bending) after the 2014 earthquake. The Iquique-Pisagua earthquake may have initiated a superinterseismic phase in the southern sector with a bimodal occurrence of megathrust events (Loveless, 2017; Melnick et al., 2017). In this case, the risk of another earthquake in this unbroken part between 21 and 23°S has increased. An opposing interpretation suggests time-dependent crustal weakening involving aseismic slip release in the Loa segment. Longer deformation time series are needed to distinguish between these hypotheses and an increased observational attention to this segment is recommended.

Acknowledgments

We thank all institutions that made GPS data available in the frame of the IPOC Network (www.ipoc-network.org; http://doi.org/10.5880/GFZ.1.1.2017.001 for cGPS data; http://doi.org/10.5880/GFZ.4.1.2017.003 for sGPS data). Data used in this study come from different institutions—German Research Centre for Geosciences, Institut de Physique du Globe de Paris, Centro Sismológico National, Universidad de Chile, Departamento de Geofísica, Proyecto Fondecyt 11140904 (CONICYT, Chile), and Universidad Cátolica del Norte, Antofagasta, Chile. We additionally acknowledge the French-Chilean International Associated Laboratory (LIA) "Montessus de Ballore" and the USA-Chilean Central Andean Tectonic Observatory Geodetic Array projects for giving access to data of several of their continuous GPS stations in Chile. We particularly thank Daniel Carrizo, Edmundo Norabuena, Diana Comte, Jorge Jara, Eduardo Contreras-Reyes, Mohamed Chlieh, Arthur Delorme, Joachim F. Genrich, Emilie Klein, Ismael Ortega, Sophie Peyrat, Efrain Rivera, Sergio Ruiz, Maria Carolina Valderas Bermejo, Klaus Dieter Bataille, Mark Simons, Anne Socquet, Christophe Vigny, and Jean-Pierre Vilotte who all contributed to the GPS data acquisition. Francisco Ortega-Culaciati acknowledges support from Proyecto Fondecyt 11140904, CONICYT, CHILE. We also thank Juan Carlos Baez (CNS Chile) and Klaus Bataille (University of Concepción, Chile) for GPS equipment. Felix Hoffmann is a member of the Helmholtz graduate research school GeoSim. Marcos Moreno has been supported by the German Science Foundation (DFG) grant MO 2310/3-1. This paper has benefitted from discussions with Jonathan Bedford. We thank two anonymous reviewers and the Associate Editor for their fruitful and useful corrections and suggestions that improved much the clarity of this study.

References

Aagaard, B., Knepley, M., & Williams, C. A. (2013). A domain decomposition approach to implementing fault slip in finite-element models of quasi-static and dynamic crustal deformation. *Journal of Geophysical Research: Solid Earth*, *118*, 3059–3079. https://doi.org/10.1002/jgrb.50217

Allmendinger, R. W., Gonzáles, G., Yu, J., Hoke, G., & Isacks, B. (2005). Trench-parallel shortening in the Northern Chilean Forearc: Tectonic and climatic implications. *Geological Society of America Bulletin*, *117*(1), 89–104. https://doi.org/10.1130/B25505.1

Allmendinger, R. W., & González, G. (2010). Tectonophysics invited review paper: Neogene to quaternary tectonics of the coastal cordillera, northern Chile. *Tectonophysics*, *495*(1–2), 93–110. https://doi.org/10.1016/j.tecto.2009.04.019

Altamimi, Z., Rebischung, P., Métivier, L., & Collilieux, X. (2016). ITRF2014: A new release of the International Terrestrial Reference Frame modeling nonlinear station motions. *Journal of Geophysical Research: Solid Earth*, *121*, 6109–6131. https://doi.org/10.1002/2016JB013098

Angermann, D., Klotz, J., & Reigber, C. (1999). Space-geodetic estimation of the Nazca-South America Euler vector. *Earth and Planetary Science Letters*, *171*(3), 329–334. https://doi.org/10.1016/S0012-821X(99)00173-9

Bedford, J., Moreno, M., Baez, J.-C., Lange, D., Tilmann, F., Rosenau, M., et al. (2013). A high-resolution, time-variable afterslip model for the 2010 Maule M_w = 8.8, Chile megathrust earthquake. *Earth and Planetary Science Letters*, *383*, 26–36. https://doi.org/10.1016/j.epsl.2013.09.020

Bedford, J., Moreno, M., Li, S., Oncken, O., Baez, J. C., Bevis, M., et al. (2016). Separating rapid relocking, afterslip, and viscoelastic relaxation: An application of the postseismic straightening method to the Maule 2010 cGPS. *Journal of Geophysical Research: Solid Earth*, *121*, 7618–7638. https://doi.org/10.1002/2016JB013093

Bedford, J., Moreno, M., Schurr, B., Bartsch, M., & Oncken, O. (2015). Investigating the final seismic swarm before the Iquique-Pisagua 2014 M_w 8.1 by comparison of continuous GPS and seismic foreshock data. *Geophysical Research Letters*, *42*, 3820–3828. https://doi.org/10.1002/2015GL063953

Béjar-Pizarro, M., Socquet, A., Armijo, R., Carrizo, D., Genrich, J., & Simons, M. (2013). Andean structural control on interseismic coupling in the North Chile subduction zone. *Nature Geoscience*, *6*(6), 462–467. https://doi.org/10.1038/ngeo1802

Bevis, M., & Brown, A. (2014). Trajectory models and reference frames for crustal motion geodesy. *Journal of Geodesy*, *88*(3), 283–311. https://doi.org/10.1007/s00190-013-0685-5

Bevis, M., Kendrick, E., Smalley, R. Jr., Brooks, B., Allmendinger, R., & Isacks, B. (2001). On the strength of interplate coupling and the rate of back arc convergence in the Central Andes: An analysis of the interseismic velocity field. *Geochemistry, Geophysics, Geosystems*, *2*, 1067. https://doi.org/10.1029/2001GC000198

Bloch, W., Kummerow, J., Salazar, P., Wigger, P., & Shapiro, S. A. (2014). High-resolution image of the North Chilean subduction zone: Seismicity, reflectivity and fluids. *Geophysical Journal International*, *197*(3), 1744–1749. https://doi.org/10.1093/gji/ggu084

Boutelier, D. A., & Oncken, O. (2010). Role of the plate margin curvature in the plateau buildup: Consequences for the central Andes. *Journal of Geophysical Research*, *115*, B04402. https://doi.org/10.1029/2009JB006296

Boutelier, D., Oncken, O., & Cruden, A. R. (2014). Trench-parallel shortening in the forearc caused by subduction along a seaward-concave plate boundary: Insights from analogue modelling experiments. *Tectonophysics*, *611*, 192–203. https://doi.org/10.1016/j.tecto.2013.11.028

Brooks, B. A., Bevis, M., Whipple, K., Arrowsmith, J. R., Foster, J., Zapata, T., et al. (2011). Orogenic-wedge deformation and potential for great earthquakes in the central Andean backarc. *Nature Geoscience*, *4*(6), 380–383. https://doi.org/10.1038/ngeo%201143

Cavalié, O., Pathier, E., Radiguet, M., Vergnolle, M., Cotte, N., Walpersdorf, A., et al. (2013). Slow slip event in the Mexican subduction zone: Evidence of shallower slip in the Guerrero seismic gap for the 2006 event revealed by the joint inversion of InSAR and GPS data. *Earth and Planetary Science Letters*, *367*, 52–60. https://doi.org/10.1016/j.epsl.2013.367.020

Cesca, S., Grigoli, F., Heimann, S., Dahm, T., Kriegerowski, M., Sobiesiak, M., et al. (2016). The M_w 8.1 2014 Iquique, Chile, seismic sequence: A tale of foreshocks and aftershocks. *Geophysical Journal International*, *204*(3), 1766–1780. https://doi.org/10.1093/gji/ggv544

Chlieh, M., De Chabalier, J. B., Ruegg, J. C., Armijo, R., Dmowska, R., Campos, J., & Feigl, K. L. (2004). Crustal deformation and fault slip during the seismic cycle in the North Chile subduction zone, from GPS and InSAR observations. *Geophysical Journal International*, *158*(2), 695–711. https://doi.org/10.1111/j.1365-246X.2004.02326.x

Chlieh, M., Perfettini, H., Tavera, H., Avouac, J. P., Remy, D., Nocquet, J. M., et al. (2011). Interseismic coupling and seismic potential along the Central Andes subduction zone. *Journal of Geophysical Research*, *116*, B12405. https://doi.org/10.1029/2010JB008166

Christensen, N. (1996). Poisson's ratio and crustal seismology. *Journal of Geophysical Research*, *101*, 3139–3156. https://doi.org/10.1029/95JB03446

Coleman, T. F., & Li, Y. (1996). A reflective Newton method for minimizing a quadratic function subject to bounds on some of the variables. *SIAM Journal on Optimization*, *6*(4), 1040–1058. https://doi.org/10.1137/S1052623494240456

Comte, D., & Pardo, M. (1991). Reappraisal of great historical earthquakes in the northern Chile and southern Peru seismic gaps. *Natural Hazards*, *4*(1), 23–44. https://doi.org/10.1007/BF00126557

Delouis, B., & Legrand, D. (2007). M_w 7.8 Tarapaca intermediate depth earthquake of 13 June 2005 (northern Chile): Fault plane identification and slip distribution by waveform inversion. *Geophysical Research Letters*, *34*, L01304. https://doi.org/10.1029/2006GL028193

Delouis, B., Pardo, M., Legrand, D., & Monfret, T. (2009). The M_w 7.7 Tocopilla earthquake of 14 November 2007 at the southern edge of the northern Chile seismic gap: Rupture in the deep part of the coupled plate interface. *Bulletin of the Seismological Society of America*, *99*(1), 87–94. https://doi.org/10.1785/0120080192

DeMets, C., Gordon, R. G., Argus, D. F., & Stein, S. (1994). Effect of recent revisions to the geomagnetic reversal time scale on estimates of current plate motions. *Geophysical Research Letters*, *21*, 2191–2194. https://doi.org/10.1029/94GL02118

Deng, Z., Gendt, G., & Schöne, T. (2016). Status of the TIGA tide gauge data reprocessing at GFZ. In C. Rizos, & P. Willis (Eds.), *IAG 150 Years: Proceedings of the IAG Scientific Assembly in Potsdam, Germany, 2013, (International Association of Geodesy Symposia; 143)* (pp. 33–40). Potsdam, Germany: Springer International. https://doi.org/10.1007/1345_2015_156

Dong, D., Fang, P., Bock, Y., Cheng, M. K., & Miyazaki, S. (2002). Anatomy of apparent seasonal variations from GPS-derived site position time series. *Journal of Geophysical Research*, *107*(B4), 2075. https://doi.org/10.1029/2001JB000573

Du, Y., Aydin, A., & Segall, P. (1992). Comparison of various inversion techniques as applied to the determination of a geophysical deformation model for the 1983 Borah Peak earthquake. *Bulletin of the Seismological Society of America*, *82*(4), 1840–1866.

Duputel, Z., Jiang, J., Jolivet, R., Simons, M., Rivera, L., Ampuero, J.-P., et al. (2015). The Iquique earthquake sequence of April 2014: Bayesian modeling accounting for prediction uncertainty. *Geophysical Research Letters*, *42*, 7949–7957. https://doi.org/10.1002/2015GL065402

Engdahl, E. R., & Villasenor, A. (2002). Global seismicity: 1900–1999. *Int. Geophys.*, *81*, 665–690. https://doi.org/10.1016/S0074-6142(02)80244-3

Geersen, J., Ranero, C. R., Barckhausen, U., & Reichert, C. (2015). Subducting seamounts control interplate coupling and seismic rupture in the 2014 Iquique earthquake area. *Nature Communications*, *6*(1), 8267–8211. https://doi.org/10.1038/ncomms9267

Geirsson, H., Árnadóttir, T., Völksen, C., Jiang, W., Sturkell, E., Villemin, T., et al. (2006). Current plate movements across the Mid-Atlantic Ridge determined from 5 years of continuous GPS measurements in Iceland. *Journal of Geophysical Research*, *111*, B09407. https://doi.org/10.1029/2005JB003717

Gendt, G., Deng, Z., Ge, M., Nischan, T., Uhlemann, M., Beeskow, G., et al. (2013). GFZ ANALYSIS CENTER OF IGS—Annual Report for 2013 (pp. 1–10).

Gephart, J. W. (1994). Topography and subduction geometry in the Central Andes: Clues to the mechanics of a noncollisional orogen. *Journal of Geophysical Research*, *99*, 12,279–12,288. https://doi.org/10.1029/94JB00129

González, G., Salazar, P., Loveless, J. P., Allmendinger, R. W., Aron, F., & Shrivastava, M. (2015). Upper plate reverse fault reactivation and the unclamping of the megathrust during the 2014 northern Chile earthquake sequence. *Geology*, *43*(8), 671–674. https://doi.org/10.1130/G36703.1

Hayes, G. P., Herman, M. W., Barnhart, W. D., Furlong, K. P., Riquelme, S., Benz, H. M., et al. (2014). Continuing megathrust earthquake potential in Chile after the 2014 Iquique earthquake. *Nature*, *512*(7514), 295–298. https://doi.org/10.1038/nature13677

Hayes, G. P., Wald, D. J., & Johnson, R. L. (2012). Slab1.0: A three-dimensional model of global subduction zone geometries. *Journal of Geophysical Research*, *117*, B01302. https://doi.org/10.1029/2011JB008524

Heki, K. (2001). Seasonal modulation of interseismic strain buildup in northeastern Japan driven by snow loads. *Science*, *293*(5527), 89–92. https://doi.org/10.1126/science.1061056

Heki, K., & Mitsui, Y. (2013). Accelerated pacific plate subduction following interplate thrust earthquakes at the Japan trench. *Earth and Planetary Science Letters*, *363*, 44–49. https://doi.org/10.1016/j.epsl.2012.12.031

Hsu, Y.-J., Simons, M., Avouac, J.-P., Galetzka, J., Sieh, K., Chlieh, M., et al. (2006). Frictional afterslip following the 2005 Nias-Simeulue earthquake, Sumatra. *Science*, *312*(5782), 1921–1926. https://doi.org/10.1126/science.1126960

Hu, Y., Bürgmann, R., Freymueller, J. T., Banerjee, P., & Wang, K. (2014). Contributions of poroelastic rebound and a weak volcanic arc to the postseismic deformation of the 2011 Tohoku earthquake. *Earth, Planets and Space*, *66*(1), 106. https://doi.org/10.1186/1880-5981-66-106

Husen, S., Kissling, E., & Flueh, E. R. (2000). Local earthquake tomography of shallow subduction in North Chile: A combined onshore and offshore study. *Journal of Geophysical Research*, *105*, 28,183–28,198. https://doi.org/10.1029/2000JB900229

Jónsson, S., Segall, P., Pedersen, R., & Björnsson, G. (2003). Post-earthquake ground movements correlated to pore-pressure transients. *Nature Geoscience*, *424*, 179–183. https://doi.org/10.1038/nature0177

Kanamori, H. (1977). The energy release in great earthquakes. *Journal of Geophysical Research*, *82*, 2981–2987. https://doi.org/10.1029/JB082i020p02981

Kaneko, Y., Avouac, J.-P., & Lapusta, N. (2010). Towards inferring earthquake patterns from geodetic observations of interseismic coupling. *Nature Geoscience*, *3*(5), 363–369. https://doi.org/10.1038/ngeo843

Kelleher, J. A. (1972). Rupture zones of large South American earthquakes and some predictions. *Journal of Geophysical Research*, *77*, 2087–2103. https://doi.org/10.1029/JB077i011p02087

King, G. C. P., Stein, R. S., & Lin, J. (1994). Static stress changes and the triggering of earthquakes. *Bulletin of the Seismological Society of America*, *84*(3), 935–953.

Klein, E., Fleitout, L., Vigny, C., & Garaud, J. D. (2016). Afterslip and viscoelastic relaxation model inferred from the large-scale post-seismic deformation following the 2010 M_w 8.8 Maule earthquake (Chile). *Geophysical Journal International*, *205*(3), 1455–1472. https://doi.org/10.1093/gji/ggw086

Klotz, J., Angermann, D., Michel, G. W., Porth, R., Reigber, C., Reinking, J., et al. (1999). GPS-derived deformation of the Central Andes including the 1995 Antofagasta M_w = 8.0 earthquake. *Pure and Applied Geophysics*, *154*(3–4), 709–730. https://doi.org/10.1007/s000240050249

Klotz, J., Khazaradze, G., Angermann, D., Reigber, C., Perdomo, R., & Cifuentes, O. (2001). Earthquake cycles dominates contemporary crustal deformation in central and southern Andes. *Earth and Planetary Science Letters*, *193*(3-4), 437–446. https://doi.org/10.1016/S0012-821X(01)00532-5

Kodaira, S., Iidaka, T., Kato, A., Park, J., Iwasaki, T., & Kaneda, Y. (2004). High Pore Fluid Pressure May Cause Silent Slip in the Nankai Trough. *Science*, *304*(5675), 1295–1298. https://doi.org/10.1126/science.1096535

Lamb, S. (2000). Active deformation in the Bolivian Andes, South America. *Journal of Geophysical Research*, *105*, 25,627–25,653. https://doi.org/10.1029/2000JB900187

Lamb, S. (2006). Shear stresses on megathrusts: Implications for mountain building behind subduction zones. *Journal of Geophysical Research*, *111*, B07401. https://doi.org/10.1029/2005JB003916

León-ríos, S., Ruiz, S., Maksymowicz, A., & Leyton, F. (2016). Diversity of the 2014 Iquique's foreshocks and aftershocks: Clues about the complex rupture process of a M_w 8. 1 earthquake. *Journal of Seismology*, *20*(4), 1059–1073. https://doi.org/10.1007/s10950-016-9568-6

Li, S., Moreno, M., Bedford, J., Rosenau, M., Heidbach, O., Melnick, D., & Oncken, O. (2017). Postseismic uplift of the Andes following the 2010 Maule earthquake: Implications for mantle rheology. *Geophysical Research Letters*, *44*, 1768–1776. https://doi.org/10.1002/2016GL071995

Li, S., Moreno, M., Bedford, J., Rosenau, M., & Oncken, O. (2015). Revisiting viscoelastic effects on interseismic deformation and locking degree: A case study of the Peru-North Chile subduction zone. *Journal of Geophysical Research: Solid Earth*, *120*, 4522–4538. https://doi.org/10.1002/2015JB011903

Loveless, J. P. (2017). Super-interseismic periods: Redefining earthquake recurrence. *Geophysical Research Letters*, *44*, 1329–1332. https://doi.org/10.1002/2017GL072525

Loveless, J. P., Allmendinger, R. W., Pritchard, M. E., Garroway, J. L., & González, G. (2009). Surface cracks record long-term seismic segmentation of the Andean margin. *Geology*, *37*(1), 23–26. https://doi.org/10.1130/G25170A.1

Lyard, F., Lefevre, F., Letellier, T., & Francis, O. (2006). Modelling the global ocean tides: Modern insights from FES2004. *Ocean Dynamics*, *56*(5–6), 394–415. https://doi.org/10.1007/s10236-006-0086-x

Marone, C. J., Scholtz, C. H., & Bilham, R. (1991). On the mechanics of earthquake afterslip. *Journal of Geophysical Research*, *96*, 8441–8452. https://doi.org/10.1029/91JB00275

Melnick, D., Moreno, M., Quinteros, J., Baez, J. C., Deng, Z., Li, S., & Oncken, O. (2017). The super-interseismic phase of the megathrust earthquake cycle in Chile. *Geophysical Research Letters*, *44*, 784–791. https://doi.org/10.1002/2016GL071845

Meng, L., Huang, H., Bürgmann, R., Ampuero, J. P., & Strader, A. (2015). Dual megathrust slip behaviors of the 2014 Iquique earthquake sequence. *Earth and Planetary Science Letters*, *411*, 177–187. https://doi.org/10.1016/j.epsl.2014.11.041

Métois, M., Socquet, A., Vigny, C., Carrizo, D., Peyrat, S., Delorme, A., et al. (2013). Revisiting the North Chile seismic gap segmentation using GPS-derived interseismic coupling. *Geophysical Journal International*, *194*(3), 1283–1294. https://doi.org/10.1093/gji/ggt183

Métois, M., Vigny, C., & Socquet, A. (2016). Interseismic coupling, Megathrust earthquakes and seismic swarms along the Chilean subduction zone (38°–18°S). *Pure and Applied Geophysics*, *173*(5), 1431–1449. https://doi.org/10.1007/s00024-016-1280-5

Métois, M., Vigny, C., Socquet, A., Delorme, A., Morvan, S., Ortega, I., & Valderas-Bermejo, C. M. (2014). GPS-derived interseismic coupling on the subduction and seismic hazards in the Atacama region, Chile. *Geophysical Journal International*, *196*(2), 644–655. https://doi.org/10.1093/gji/ggt418

Metzger, S., Jónsson, S., Danielsen, G., Hreinsdóttir, S., Jouanne, F., Giardini, D., & Villemin, T. (2013). Present kinematics of the Tjörnes fracture zone, North Iceland, from campaign and continuous GPS measurements. *Geophysical Journal International*, *192*(2), 441–455. https://doi.org/10.1093/gji/ggs032

Moreno, M, Bedford, J., Baez, J.-C., Klotz, J., Hoffmann, F., Deng, Z., et al. (2017). Survey mode GPS data in the IPOC Region, Central Andes, Chile, GFZ Data Services. https://doi.org/10.5880/GFZ.4.1.2017.003

Moreno, M., Melnick, D., Rosenau, M., Bolte, J., Klotz, J., Echtler, H., et al. (2011). Heterogeneous plate locking in the south-central Chile subduction zone: Building up the next great earthquake. *Earth and Planetary Science Letters*, *305*(3–4), 413–424. https://doi.org/10.1016/j.epsl.2011.03.025

Moreno, M., Rosenau, M., & Oncken, O. (2010). 2010 Maule earthquake slip correlates with pre-seismic locking of Andean subduction zone. *Nature*, *467*(7312), 198–202. https://doi.org/10.1038/nature09349

Motagh, M., Schurr, B., Anderssohn, J., Cailleau, B., Walter, T. R., Wang, R., & Villotte, J. P. (2010). Subduction earthquake deformation associated with 14 November 2007, M_w 7.8 Tocopilla earthquake in Chile: Results from InSAR and aftershocks. *Tectonophysics*, *490*(1-2), 60–68. https://doi.org/10.1016/j.tecto.2010.04.033

Nishenko, S. P. (1985). Seismic potential for large and great interplate earthquakes along the Chilean and southern Peruvian margins of South America: A quantitative reappraisal. *Journal of Geophysical Research*, *90*, 3589–3615. https://doi.org/10.1029/JB090iB05p03589

Nur, A., & Mavko, G. (1974). Postseismic viscoelastic rebound. *Science*, *183*(4121), 204–206. https://doi.org/10.1126/science.183.4121.204

Okada, Y. (1992). Internal deformation due to shear and tensile faults in a half-space. *Bulletin of the Seismological Society of America*, *97*(B5), 7137–1040. https://doi.org/10.1029/92JB00178

Peltzer, G., Rosen, P., Rogez, F., & Hudnut, K. (1998). Poroelastic rebound along the Landers 1992 earthquake surface rupture. *Journal of Geophysical Research*, *103*, 30,131–30,145. https://doi.org/10.1029/98JB02302

Perfettini, H., Avouac, J.-P., Tavera, H., Kositsky, A., Nocquet, J.-M., Bondoux, F., et al. (2010). Seismic and aseismic slip on the Central Peru megathrust. *Nature*, *465*(7294), 78–81. https://doi.org/10.1038/nature09062

Rebischung, P., Ray, J., Benoist, C., Metivier, L., & Altamimi, Z. (2015). Error analysis of the IGS repro2 station position time series (13 pp.). Abstract G23B-1065 Presented at the 2015 AGU Fall Meeting, San Francisco, CA.

Reutter, K.-J., Scheuber, E., & Wigger, P. (Eds.) (1994). *Tectonics of the southern Central Andes* (334 pp.). Heidelberg: Springer-Verlag. https://doi.org/10.1007/978-3-642-77353-2

Rietbrock, A., & Waldhauser, F. (2004). A narrowly spaced double-seismic zone in the subducting Nazca Plate. *Geophysical Research Letters*, *31*, L10608. https://doi.org/10.1029/2004GL019610

Ruegg, J. C., Campos, J., Armijo, R., Barrientos, S., Briole, P., Thiele, R., et al. (1996). The M_w = 8.1 Antofagasta (North Chile) earthquake of July 30,1995: First results from teleseismic and geodetic data. *Geophysical Research Letters*, *23*, 917–920. https://doi.org/10.1029/96GL01026

Ruegg, J. C., Olcay, M., & Lazo, D. (2001). Co-, post- and pre(?)-seismic displacements associated with the M_w8.4 southern Peru earthquake of 23 June 2001 from continuous GPS measurements. *Seismological Research Letters*, *72*(6), 673–678. https://doi.org/10.1785/gssrl.72.6.673

Ruiz, S., Métois, M., Fuenzalida, A., Ruiz, J., Leyton, F., Grandin, R., et al. (2014). Intense foreshocks and a slow slip event preceded the 2014 Iquique M_w 8.1 earthquake. *Science*, *345*(6201), 1165–1169. https://doi.org/10.1126/science.1256074

Savage, J. C. (1983). A dislocation model of strain accumulation and release at a subduction zone. *Journal of Geophysical Research*, *88*(B6), 4984–4996. https://doi.org/10.1029/JB088iB06p04984

Schmid, R., Steigenberger, P., Gendt, G., Ge, M., & Rothacher, M. (2007). Generation of a consistent absolute phase-center correction model for GPS receiver and satellite antennas. *Journal of Geodesy*, *81*(12), 781–798. https://doi.org/10.1007/s00190-007-0148-y

Scholz, C. H. (1998). Earthquakes and friction laws. *Nature*, *391*(6662), 37–42. https://doi.org/10.1038/34097

Schurr, B., Asch, G., Hainzl, S., Bedford, J., Hoechner, A., Palo, M., et al. (2014). Gradual unlocking of plate boundary controlled initiation of the 2014 Iquique earthquake. *Nature*, *512*(7514), 299–302. https://doi.org/10.1038/nature13681

Simons, M., Galetzka, J. E., Genrich, J. F., Ortega, F., Comte, D., Glass, B., et al. (2010). Central Andean tectonic observatory geodetic Array, UNAVCO, GPS Data Set. https://doi.org/10.7283/T50P0X37

Sippl, C., Schurr, B., Asch, G., & Kummerow, J. (2018). Seismicity structure of the Northern Chile forearc from >100 000 double-difference relocated hypocenters. *Journal of Geophysical Research: Solid Earth*, *123*. https://doi.org/10.1002/2017JB015384

Sippl, C., Schurr, B., Yuan, X., Mechie, J., Schneider, F. M., Gadoev, M., et al. (2013). Geometry of the Pamir-Hindu Kush intermediate-depth earthquake zone from local seismic data. *Journal of Geophysical Research: Solid Earth*, *118*, 1438–1457. https://doi.org/10.1002/jgrb.50128.7

Tassara, A., & Echaurren, A. (2012). Anatomy of the Andean subduction zone: Three-dimensional density model upgraded and compared against global-scale models. *Geophysical Journal International*, *189*(1), 161–168. https://doi.org/10.1111/j.1365-246X.2012.05397.x

Tilmann, F., Zhang, Y., Moreno, M., Saul, J., Eckelmann, F., Palo, M., et al. (2016). The 2015 Illapel earthquake, Central Chile: A type case for a characteristic earthquake? *Geophysical Research Letters*, *43*, 574–583. https://doi.org/10.1002/2015GL066963

Trubienko, O., Fleitout, L., Garaud, J. D., & Vigny, C. (2013). Interpretation of interseismic deformations and the seismic cycle associated with large subduction earthquakes. *Tectonophysics*, *589*, 126–141. https://doi.org/10.1016/j.tecto.2012.12.027

Van Dam, T., Wahr, J., Milly, P. C. D., Shmakin, A. B., Blewitt, G., Lavallée, D., & Larson, K. M. (2001). Crustal displacements due to continental water loading. *Geophysical Research Letters*, *28*, 651–654. https://doi.org/10.1029/2000GL012120

Wang, K., & Bilek, S. L. (2011). Do subducting seamounts generate or stop large earthquakes? *Geology*, *39*(9), 819–822. https://doi.org/10.1130/G31856.1

Wang, K., Hu, Y., & He, J. (2012). Deformation cycles of subduction earthquakes in a viscoelastic Earth. *Nature*, *484*(7394), 327–332. https://doi.org/10.1038/nature11032

Weiss, J. R., Brooks, B. A., Foster, J. H., Bevis, M., Echalar, A., Caccamise, D., et al. (2016). Isolating active orogenic wedge deformation in the southern Subandes of Bolivia. *Journal of Geophysical Research: Solid Earth*, *121*, 6192–6218. https://doi.org/10.1002/2016JB013070

Yagi, Y., Okuwaki, R., Enescu, B., Hirano, S., Yamagami, Y., Endo, S., & Komoro, T. (2014). Rupture process of the 2014 Iquique Chile earthquake in relation with the foreshock activity. *Geophysical Research Letters*, *41*, 4201–4206. https://doi.org/10.1002/2014GL060274

Yoon, M., Buske, S., Shapiro, S. A., & Wigger, P. (2009). Reflection image spectroscopy across the Andean subduction zone. *Tectonophysics*, *472*(1–4), 51–61. https://doi.org/10.1016/j.tecto.2008.03.014